Analysis of the lattice Boltzmann Bhatnagar-Gross-Krook no-slip boundary condition: Ways to improve accuracy and stability

Joris C. G. Verschaeve*

Department of Energy and Process Engineering, Norwegian University of Science and Technology, N-7491 Trondheim, Norway

(Received 26 June 2008; revised manuscript received 22 May 2009; published 11 September 2009)

An analytical and numerical analysis of the no-slip boundary condition at walls at rest for the lattice Boltzmann Bhatnagar-Gross-Krook method is performed. The main result of this analysis is an alternative formulation for the no-slip boundary condition at walls at rest. Numerical experiments assess the accuracy and stability of this formulation for Poiseuille and Womersley flows, flow over a backward facing step, and unsteady flow around a square cylinder. This no-slip boundary condition is compared analytically and numerically to the boundary conditions of Inamuro *et al.* [Phys. Fluids **7**, 2928 (1995)] and Zou and He [Phys. Fluids **9**, 1591 (1997)] and it is found that all three make use of the same mechanism for the off-diagonal element of the stress tensor. Mass conservation, however, is only assured by the present one. In addition, our analysis points out which mechanism lies behind the instabilities also observed by Lätt *et al.* [Phys. Rev. E **77**, 056703 (2008)] for this kind of boundary conditions. We present a way to remove these instabilities, allowing one to reach relaxation frequencies considerably closer to 2.

DOI: 10.1103/PhysRevE.80.036703 PACS number(s): 47.11.−j, 05.20.Dd

I. INTRODUCTION

The lattice Boltzmann method has become increasingly popular for computing fluid flows [1–3]. It is based on a particle approach, meaning that a fluid is rather considered as an ensemble of particles than as continuous matter. These particles can travel from one grid node to the other, where they undergo collisions with each other. These two principles are materialized in the streaming and collision step of the lattice Boltzmann method. Macroscopic quantities, such as density or momentum, are then recovered as statistical moments of the particle distribution function, the central object of the lattice Boltzmann method. From a numerical point of view, the lattice Boltzmann method is a second-order scheme in space and time if compressibility effects can be made negligible.

As mentioned in [4], boundary conditions are still an open issue. Rather than focusing on the general velocity boundary condition, the present discussion treats a particular case, namely, the no-slip condition at walls at rest, meaning that the viscous fluid has the same velocity at the wall as the wall itself, namely, zero.

The difficulty of boundary conditions in lattice Boltzmann methods is to find a formulation for the particle distribution functions leaving into the bulk-fluid domain, but which do not stem from the computational domain. The lattice Boltzmann boundary conditions can be divided into two families, the bounce back [5] and the so-called wet boundary conditions [6]. For the former, boundary nodes lie outside of the fluid domain, whereas for the latter ones, they are infinitesimally close to the boundary but still part of the fluid domain. Therefore the former ones only formulate a closure for the unknown populations, whereas the later ones still apply a collision step before streaming, similar to a bulk node.

The bounce back rule is traditionally used for no-slip boundary conditions since it assures mass conservation and zero velocity at the boundary. In addition, it is very simple to implement from a programming point of view and stable for relaxation frequencies close to 2. It has been the object of intense study during the last years [5,7,8]. Therefore the present discussion treats the no-slip condition for a wall at rest modeled by wet boundary conditions. A drawback of the bounce back rule is that for straight boundaries, the location of the wall is at half-way between the wall node and the first fluid node. This grid dependence can be circumvented by adding an extra node in wall normal direction when, for example, dealing with a channel. Unfortunately, the points at which the flow is computed do change with the resolution of the grid. In addition, Inamuro *et al.* [8] showed that depending on the relaxation frequency ω the flow can exhibit a nonzero velocity at the wall. Rather than focusing on these points, much effort has been spent on finding formulations for arbitrary wall positions and wall shapes, thereby sacrificing the nonlocality and mass conservation [9,10]. An interesting approach has been proposed by [11] recovering parts of the advantages.

In order to locate the wall directly at the boundary node, wet boundary conditions are often employed as no-slip conditions. They can, however, be used for more general purposes such as inflow and outflow boundary conditions [4,12]. Wet boundary conditions can be divided into two groups, the local and the nonlocal versions. Local versions [8,12] use information from the ingoing particle distribution functions on the boundary node itself, whereas nonlocal boundary conditions [4,5] use additional information from next neighbors and nearest-next neighbors. These boundary conditions do not deteriorate the second-order accuracy of the lattice Boltzmann method. Nevertheless, a general disadvantage of wet boundary conditions as no-slip condition is their lack of mass conservation. In addition, as stated in [4], the local versions become unstable for values of the relaxation frequency close to 2.

The present discussion derives a local wet boundary condition for the particular but important case of straight no-slip

*joris.verschaeve@ntnu.no

 ©2009 The American Physical Society

boundary conditions for walls at rest, removing the drawback of mass loss and instability by using additional physical arguments. More precisely two no-slip boundary conditions are derived, one highly accurate, which is stable for lower values of the relaxation frequency, and one, slightly less accurate but stable for values of the relaxation frequency close to 2. In addition, we compare these boundary conditions analytically and numerically to other wet boundary conditions, thereby elucidating the principles behind accuracy and stability of the wet boundary condition.

We present some general aspects of the lattice Boltzmann method in Sec. II. The boundary conditions we compare the present no-slip conditions to are presented in Sec. III. The derivation of the present boundary conditions is done in Sec. IV. A short analysis of the nature of the instabilities is found in Sec. V A of the numerical verification (Sec. V). The numerical verification consists of four different benchmark tests of increasing complexity. The first benchmark test is steady Poiseuille flow in Sec. V C. For the case of a simple unsteady flow, the Womersley flow is used (cf. Sec. V D). The results of the third benchmark test, a backward facing step flow at Re=800, are presented in Sec. V E. The unsteady flow around a square cylinder at Re=100 in Sec. V F concludes the numerical verification. An analysis of the present no-slip and the other local wet boundary conditions for the no-slip case is performed in Sec. VI, revealing the mechanisms concerning accuracy and stability which are common to all these boundary conditions. Finally, the present discussion is concluded in Sec. VII.

II. LATTICE BOLTZMANN BHATNAGAR-GROSS-KROOK

This section presents the main elements of the lattice Boltzmann method necessary for the present discussion. We treat only the lattice Boltzmann Bhatnagar-Gross-Krook (LBGK) version of the lattice Boltzmann method. For a more detailed introduction to the lattice Boltzmann method and LBGK in particular, we refer to [1–3]. The central object of the lattice Boltzmann method is the "particle" distribution function $f(t,\vec{x},\vec{c})$ which is a function of time t, the position $\vec{x}$, and the particle velocity $\vec{c}$. It corresponds to the probability of finding a particle at a given position $\vec{x}$ with a given velocity $\vec{c}$. In its discrete form, the velocities a particle can travel with are limited to a very small number $\vec{c}_i$, $i=0,\ldots,q-1$, for instance, in the D2Q9 lattice, the lattice used throughout this discussion (see Fig. 1 and Table I), a particle can only have one out of nine discrete velocities. These velocities are not arbitrary but chosen in such a way that the system is isotropic and that the velocities are interconnecting the grid nodes of the computational domain. The computational grid and the ensemble of velocities are called a lattice. In addition, lattice weights t_i, $i=0,\ldots,q-1$, are associated to all discrete velocities $\vec{c}_i$, accounting for the difference in length of the lattice vectors. For the D2Q9 lattice the lattice weights t_i and lattice velocities $\vec{c}_i$ are defined in Table I. A fundamental condition is that a particle travels exactly the distance Δx, the grid spacing, during one time step Δt. Therefore the particle speed or lattice constant c is given by

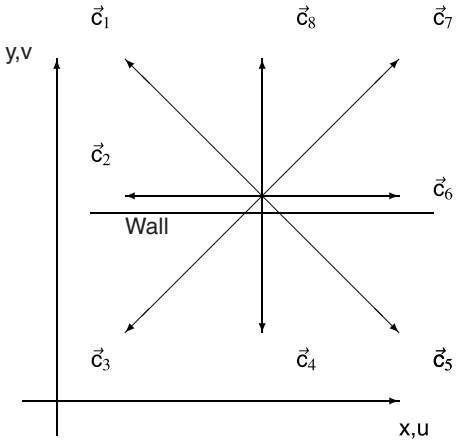

FIG. 1. The D2Q9-lattice node and its position at the wall.

$$c = \frac{\Delta x}{\Delta t}. \tag{2.1}$$

For a number of lattices the speed of sound c_s is related to the lattice constant by

$$c_s = \frac{c}{\sqrt{3}}. \tag{2.2}$$

Usually the system of units is chosen such that

$$\Delta x = \Delta t = c = 1. \tag{2.3}$$

When referring to the grid spacing or time step in its actual physical units we use a lower case δ instead, for example, if we choose the characteristic length L to be 1 and we use $N+1$ points to resolve this length then we have $\delta x = 1/N$.

With the discrete set of particle velocities, the distribution function $f(t,\vec{x},\vec{c})$ can then be written as follows:

$$f(t,\vec{x},\vec{c}) = \begin{cases} f_0(t,\vec{x}) & \text{if } \vec{c}=\vec{c}_0 \\ \vdots & \vdots \\ f_i(t,\vec{x}) & \text{if } \vec{c}=\vec{c}_i \\ \vdots & \vdots \\ f_{q-1}(t,\vec{x}) & \text{if } \vec{c}=\vec{c}_{q-1} \\ 0 & \text{else,} \end{cases} \tag{2.4}$$

where f_i is called a population. This leads to q equations, the so-called lattice Boltzmann equation, taking the following form:

$$f_i(t+1,\vec{x}+\vec{c}_i) = f_i(t,\vec{x}) + \Omega_i, \tag{2.5}$$

where Ω_i is the collision operator accounting for the effect of the collisions particles undergo at the lattice nodes. Equation (2.5) can be divided into two steps: collision and streaming. If we denote the populations before collision with the superscript *in* and the populations after collision with the superscript *out* then Eq. (2.5) can be rewritten as follows:

$$f_i^{out}(t,\vec{x}) = f_i^{in}(t,\vec{x}) + \Omega_i, \tag{2.6}$$

TABLE I. The lattice velocities $\vec{c}_i$ and lattice weights t_i of the D2Q9 lattice.

i	0	1	2	3	4	5	6	7	8
t_i	4/9	1/36	1/9	1/36	1/9	1/36	1/9	1/36	1/9
$\vec{c}_i$	(0,0)	(−1,1)	(−1,0)	(−1,−1)	(0,−1)	(1,−1)	(1,0)	(1,1)	(0,1)

$$f_i^{in}(t+1,\vec{x}+\vec{c}_i) = f_i^{out}(t,\vec{x}). \tag{2.7}$$

The collision step is local whereas the streaming step is nonlocal and corresponds to the propagation of particles after collision to neighboring nodes. Sometimes we will also use the superscript *ps* for poststreamed populations. That is to say, after all populations have been streamed to the neighboring nodes, we apply a so-called repopulation or reconstruction step changing the poststreamed populations into *in* populations. For bulk nodes the repopulation step is identical to the identity operation, more precisely for LBGK, but at boundary nodes this is not necessarily the case. For notational convenience the superscript *in* will often be dropped. During collision, mass and momentum are conserved. The collision operator is usually defined in terms of a relaxation of the populations f_i toward an equilibrium distribution f_i^{eq}, the BGK operator,

$$\Omega_i = -\omega(f_i - f_i^{eq}), \tag{2.8}$$

where ω is called the relaxation frequency. The most common choice for the equilibrium function is a low Mach number expansion of the Maxwell distribution,

$$f_i^{eq}(\rho,\vec{u}) = t_i\rho\left(1 + \frac{1}{c_s^2}\vec{c}_i\cdot\vec{u} + \frac{1}{2c_s^4}\mathbf{Q}_i{:}\vec{u}\vec{u}\right), \tag{2.9}$$

where the tensor $\mathbf{Q}_i$ is defined as follows:

$$\mathbf{Q}_i = \vec{c}_i\vec{c}_i - c_s^2\mathbf{I}.$$

Macroscopic quantities such as density ρ or flow velocity $\vec{u}$ are given by the statistical moments of the distribution function and their linear combinations,

(i) density

$$\rho = \sum_i f_i, \tag{2.10}$$

(ii) momentum

$$\vec{j} = \rho\vec{u} = \sum_i \vec{c}_i f_i, \tag{2.11}$$

(iii) second-order tensor

$$\mathbf{\Pi} = \sum_i \vec{c}_i\vec{c}_i f_i.$$

The standard procedure to derive the governing equations for these macroscopic quantities is called the Chapman-Enskog multiscale analysis [3]. The central idea of the Chapman-Enskog multiscale analysis is that the populations can be developed into a power series of a small quantity ϵ which is identified with the Knudsen number, the ratio between the mean free path and the reference length [1,3,13],

$$f_i = f_i^{(0)} + \epsilon f_i^{(1)} + \cdots.$$

The zeroth-order term of this series is taken to be the equilibrium distribution. The difference $f_i^{neq} = f_i - f_i^{eq}$ is usually referred to as the nonequilibrium part. It is to first order equal to $\epsilon f_i^{(1)}$. In order to conserve mass during collision the sum of the nonequilibrium parts has to be zero,

$$\sum_i f_i^{neq} = 0. \tag{2.12}$$

Similarly, the conservation of momentum requires that

$$\sum_i \vec{c}_i f_i^{neq} = \vec{0}. \tag{2.13}$$

The multiscale analysis leads to an expression for the first-order term of the populations,

$$f_i^{(1)} = -\frac{t_i}{c_s^2\omega}\left(\mathbf{Q}_i{:}\rho\nabla\vec{u} - \vec{c}_i\nabla{:}\rho\vec{u}\vec{u} + \frac{1}{2c_s^2}(\vec{c}_i\cdot\nabla)(\mathbf{Q}_i{:}\rho\vec{u}\vec{u})\right). \tag{2.14}$$

A result of the multiscale analysis is that macroscopic quantities obey the incompressible Navier-Stokes equations for small Mach and Knudsen numbers [1,3],

$$\nabla\cdot\vec{u} = 0, \tag{2.15}$$

$$\partial_t\rho\vec{u} + \nabla\cdot(\rho\vec{u}\vec{u}) = -\nabla p + \nabla\cdot\tau, \tag{2.16}$$

where the pressure p is given by the equation of state of an ideal gas,

$$p = c_s^2\rho,$$

and the stress tensor τ is defined as

$$\tau = 2\nu\rho\mathbf{S}.$$

The kinematic viscosity can then be related to the relaxation frequency ω,

$$\nu = c_s^2\left(\frac{1}{\omega} - \frac{1}{2}\right).$$

The rate of strain tensor $\mathbf{S} = [\nabla\vec{u} + (\nabla\vec{u})^T]/2$ is given by the sum of $\vec{c}_i\vec{c}_i$ and the first-order part of the populations,

$$\Pi^{(1)} = \sum_i \vec{c}_i\vec{c}_i f_i^{(1)} = -\frac{2c_s^2}{\omega}\rho\mathbf{S}. \tag{2.17}$$

We remark that Eqs. (2.14)–(2.16) are solved by the scheme up to an error composed of three contributions:

(i) The spatial error scales like δx^2, where δx is the grid spacing.

(ii) The temporal error scales like δt^2, where δt is the time step.

(iii) The compressibility error scales like Ma^2, where Ma is the Mach number.

Therefore, we say that the incompressible Navier-Stokes equations are recovered up to second order. In the present discussion, we will make use of the expression "up to second order," meaning that an equation contains the above error. In the Chapman-Enskog expansion only $\Pi^{(1)}$ enters into the derivations of the hydrodynamic equations instead of $f_i^{(1)}$ alone. This fact has been used by Lätt to develop a method reconstructing the populations from the pure knowledge of ρ, $\vec{u}$, and $\mathbf{S}$ on the node by first computing these quantities and then the nonequilibrium part of the populations by

$$f_i^{neq} \approx -\frac{\rho t_i}{c_s^2 \omega} \mathbf{Q}_i : \mathbf{S} \tag{2.18}$$

and finally reconstructing the populations by using

$$f^{in} = f_i^{eq} + f_i^{neq}. \tag{2.19}$$

This procedure is called the regularized lattice Boltzmann method [14]. Lätt's reconstruction method will be used for the finite difference (FD) boundary conditions presented in Sec. III which are also used to impose the inflow and outflow boundary conditions throughout the present discussion. The present no-slip boundary condition, presented in Sec. IV, makes equally use of Eq. (2.19) but finds the nonequilibrium part f_i^{neq} locally and not by Eq. (2.18). In the bulk fluid, a usual LBGK collision step is performed.

III. SHORT OVERVIEW OF WET BOUNDARY CONDITIONS FOR LBGK

We restrict ourselves to the two-dimensional case, more precisely the D2Q9 lattice (cf. Fig. 1 and Table I). For demonstrative purposes we concentrate on a flat wall at rest which is situated at the south of our computational domain. For all numerical simulations in the present discussion, the FD boundary condition in [4] was used as velocity inflow and pressure outlet. These boundary conditions together with the boundary conditions of Zou and He [12] and Inamuro *et al.* [8] can be used for arbitrary velocities. The no-slip condition is in this sense only a particular choice of the velocity on the boundary. However, they are often used as no-slip boundary conditions because of their superior accuracy to the bounce back rule. We briefly present these three boundary conditions.

A. Boundary condition of Zou and He

Provided that the density on the wall is given by Eq. (2.10) and the velocity by Eq. (2.11), we can solve these three equations for the unknown populations, f_1^{in}, f_7^{in}, and f_8^{in},

$$f_1^{in} + f_7^{in} + f_8^{in} = \rho - (f_0^{in} + f_2^{in} + f_3^{in} + f_4^{in} + f_5^{in} + f_6^{in}), \tag{3.1}$$

$$f_7^{in} - f_1^{in} = \rho u - (f_6^{in} - f_2^{in} + f_5^{in} - f_3^{in}), \tag{3.2}$$

$$f_1^{in} + f_7^{in} + f_8^{in} = \rho v + (f_3^{in} + f_4^{in} + f_5^{in}). \tag{3.3}$$

From Eqs. (3.1) and (3.3) we can determine the density at the wall,

$$\rho = \frac{f_0^{in} + f_2^{in} + f_6^{in} + 2(f_3^{in} + f_4^{in} + f_5^{in})}{1 - v}. \tag{3.4}$$

However one equation is still missing in order to close the system. Zou and He [12] suggested that the nonequilibrium part of the incoming normal population should be bounced back into the bulk, i.e., $f_8^{neq} = f_4^{neq}$. By help of this condition Eqs. (3.2) and (3.3) can be solved for the remaining unknowns f_1^{in} and f_7^{in}.

B. Boundary condition of Inamuro *et al.*

The boundary condition of Inamuro *et al.* [8] is based on a result of kinetic theory stating that for particles colliding with a wall the outgoing particle distribution function is a Maxwellian centered around the velocity of the wall (diffuse reflection). For LBGK the equivalent equilibrium particle distribution is used. The outgoing populations are thus equilibrium distributions with a *counterslip density* ρ' and a *counterslip velocity* u', along x in the present case, such that the resulting velocity is the velocity of the wall $\vec{u}^{wall}$. In principle this amounts at rewriting the unknown populations as functions of the unknown parameters ρ' and u',

$$f_i^{in} = f_i^{eq}(\rho', \vec{u}^{wall} + u' \vec{e}_x), \quad i = 1,7,8, \tag{3.5}$$

where $\vec{e}_x = (1,0)^T$ is the unit vector in x direction. Then ρ' and u' are solved from the condition that the velocity at the node has to equal the wall velocity $\vec{u}^{wall}$,

$$\sum_i \vec{c}_i f_i^{in} = \rho^{wall} \vec{u}^{wall}, \tag{3.6}$$

where the density ρ^{wall} is given by

$$\rho^{wall} = \sum_i f_i^{in}. \tag{3.7}$$

C. Finite difference boundary conditions

This boundary condition [4] is based on a different approach than the former two. Apart from the wall density no information is sought to be obtained from the boundary node itself, instead, the idea behind this boundary condition is to find an estimate of the stress tensor and to determine all populations on the node by regularization formula (2.19). In order to interpolate the velocity gradient, next-neighbor and nearest-next-neighbor nodes are used. Therefore this boundary condition is nonlocal, in contrary to the preceding two. From this gradient estimate the rate of strain tensor $\mathbf{S}$ is computed. The density ρ on the other hand is determined locally by formula (3.4). Using ρ, the imposed velocity and the rate of strain tensor $\mathbf{S}$, all populations on the node are reconstructed by Eq. (2.19).

Due to the importance of the external corner (Fig. 2) for the third benchmark test (cf. Sec. V E), we discuss the generic formulation of the external corner by Lätt *et al.* [4,15] which is used for all boundary conditions except the present one. It implements the corner treatment the following way.

After streaming, all populations are known, except for f_7. The density on the node is computed as an arithmetic aver-

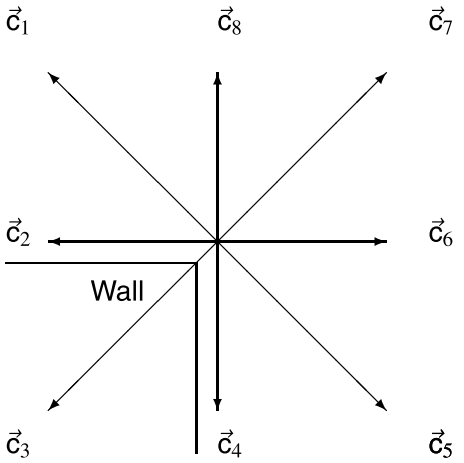

FIG. 2. Position of the D2Q9-lattice node at the external corner.

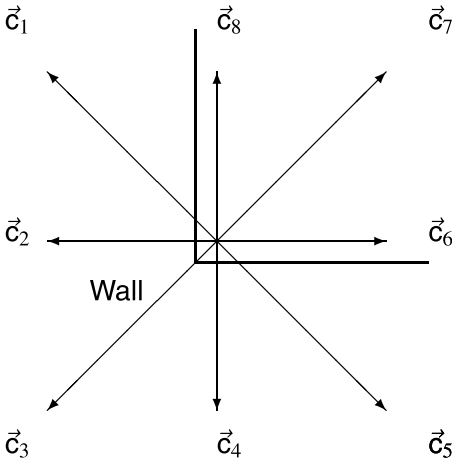

FIG. 3. Position of the D2Q9-lattice node at the internal corner.

age of formula (3.4) in y and in x directions, explicitly this means

$$\rho^{wall} = f_0^{in} + f_1^{in} + \tfrac{3}{2}f_2^{in} + 2f_3^{in} + \tfrac{3}{2}f_4^{in} + f_5^{in} + \tfrac{1}{2}f_6^{in} + \tfrac{1}{2}f_8^{in}. \tag{3.8}$$

The unknown nonequilibrium part f_7^{neq} is then taken equal to f_3^{neq}. Then, the rate of strain tensor is computed on the node by Eq. (2.17) and the populations are reconstructed by the regularization procedure [14] [formula (2.19)]. Finally the usual BGK collision step is performed. The formulation of Lätt *et al.* is very robust but does not guarantee mass conservation.

In contrary to the FD boundary condition, the no-slip boundary condition, derived in Sec. IV, uses only local information, but unlike the boundary condition of Inamuro *et al.* and Zou and He, the populations coming from bulk nodes and from boundary nodes are treated differently.

IV. NO-SLIP BOUNDARY CONDITION FOR LBGK

We precede the derivation (Sec. IV C) of the present boundary conditions with some results for the rate of strain tensor at the no-slip boundary by hydrodynamic considerations (Sec. IV A) and show the direct implications for the distribution functions in Sec. IV.

A. Hydrodynamic implications at the no-slip boundary

According in [16], the no-slip boundary condition for a fluid at a southern wall along x, as sketched in Fig. 1, implies that the derivatives along x of the velocity components u and v are zero at the wall,

$$\partial_x u = \partial_x v = 0. \tag{4.1}$$

Due to continuity [Eq. (2.15)], this leads to

$$\partial_y v = 0 \tag{4.2}$$

at the wall. Therefore two elements of the rate of strain tensor are already determined by the no-slip boundary condition,

$$S_{xx} = S_{yy} = 0. \tag{4.3}$$

For an external corner as depicted in Fig. 2 we know that to the left-hand side of the corner we have

$$\partial_x u = \partial_x v = \partial_y v = 0. \tag{4.4}$$

To the right-hand side, following the western wall downward,

$$\partial_y u = \partial_y v = \partial_x u = 0 \tag{4.5}$$

must hold true. Taking now the limit from both sides, we see that immediately at the corner

$$\partial_x u = \partial_x v = \partial_y u = \partial_y v = 0. \tag{4.6}$$

This is also valid for the internal corner (Fig. 3). An example of an application of this general result can be found in [17], p. 61. These implications follow naturally when imposing the no-slip condition at the boundary for a numerical scheme solving the incompressible Navier-Stokes equation directly. However, for a lattice Boltzmann method this is not true. As example one can cite the equilibrium boundary condition which imposes the equilibrium distribution on the outgoing links at the boundary node using the known values of ρ and $\vec{u}$ (for this special case $f_i^{neq}=0$, $i=0,\ldots,8$). This boundary condition has been discussed in [4] and it has been shown that even for a Poiseuille flow, for which the analytical pressure is known and can be used to determine ρ, this boundary condition leads to inaccurate results. This motivates the search for a more accurate formulation for the populations going out from the boundary node onto fluid nodes. We will see in the next sections how the rate of strain tensor can help us to find an accurate closure.

Another, although more qualitative fact can be obtained from continuous hydrodynamics. We know that for a flow at a Reynolds number $\mathrm{Re} > 1$, the physics is dominated by convection at the interior of the fluid domain, whereas at the boundary the role of diffusion becomes increasingly important as $\vec{u}$ goes to zero.

B. Implications for the leading order term of the nonequilibrium parts

In Sec. IV A it was shown that the only nonzero element of the rate of strain tensor at a straight southern wall along x is the off-diagonal S_{xy}. Applying this result to the expression for f_i^{neq} obtained by the Chapman-Enskog expansion [Eq. (2.14)], we see that up to second order the nonequilibrium parts of our populations are given by

$$f_i^{neq} = 0, \quad i = 0,2,4,6,8, \tag{4.7}$$

$$f_i^{neq} = \frac{2t_i\rho}{c_s^2\omega} S_{xy}, \quad i = 1,5, \tag{4.8}$$

$$f_i^{neq} = -\frac{2t_i\rho}{c_s^2\omega} S_{xy}, \quad i = 3,7. \tag{4.9}$$

In Sec. IV C a method is proposed to find a local closure of the unknown particle distribution functions by exploiting the implications of the rate of strain but additionally using local information.

C. Derivation

We start our derivation with considerations about mass conservation at the boundary node.

1. Mass conservation

First, we concentrate on a straight wall at the south of our computational domain (Fig. 1). A discussion of the corners follows (Figs. 2 and 3).

2. Straight wall

Hollis *et al.* [18] required mass conservation at the boundary by imposing that the total mass on the boundary node coming from nodes of the computational domain after streaming, m^{ps}, should equal the total mass streamed onto nodes of the computational domain from the boundary node after collision, m^{out}. For the boundary node depicted in Fig. 1, m^{ps} and m^{out} are given by

$$m^{ps} = \sum_{i \neq 1,7,8} f_i^{ps}, \tag{4.10}$$

$$m^{out} = \sum_{i \neq 3,4,5} f_i^{out}. \tag{4.11}$$

The mass conservation condition reads then

$$m^{out} = m^{ps}. \tag{4.12}$$

Chopard and Dupuis [19], on the other hand, required that the mass leaving the bulk-fluid domain should re-enter it after one time step. For this case m^{ps} and m^{out} are given by

$$m^{ps} = f_3^{ps} + f_4^{ps} + f_5^{ps}, \tag{4.13}$$

$$m^{out} = f_1^{out} + f_8^{out} + f_7^{out}. \tag{4.14}$$

The mass conservation condition reads similarly

$$m^{out} = m^{ps}. \tag{4.15}$$

The latter version of Chopard and Dupuis realizes mass conservation from a fluid perspective, whereas Hollis *et al.* adopted mass conservation from a fluid-boundary perspective since the populations from the boundary node are included in the mass budget.

3. External corner

The external corner is similar. Here, we have for the fluid-boundary perspective the following condition:

$$m^{ps} = \sum_{i \neq 7} f_i^{ps}, \tag{4.16}$$

$$m^{out} = \sum_{i \neq 3} f_i^{out}, \tag{4.17}$$

$$m^{out} = m^{ps}. \tag{4.18}$$

In the fluid perspective we require

$$m^{ps} = \sum_{i=1,2,3,4,5} f_i^{ps}, \tag{4.19}$$

$$m^{out} = \sum_{i=1,5,6,7,8} f_i^{out}, \tag{4.20}$$

$$m^{out} = m^{ps}. \tag{4.21}$$

4. Internal corner

For an internal corner (Fig. 3), mass conservation condition of Hollis *et al.* reads

$$m^{ps} = \sum_{i \neq 1,5,6,7,8} f_i^{ps}, \tag{4.22}$$

$$m^{out} = \sum_{i \neq 1,2,3,4,5} f_i^{out}, \tag{4.23}$$

$$m^{out} = m^{ps}. \tag{4.24}$$

The Chopard-Dupuis fluid perspective requires instead that

$$m^{ps} = f_3^{ps}, \tag{4.25}$$

$$m^{out} = f_7^{out}, \tag{4.26}$$

$$m^{out} = m^{ps}. \tag{4.27}$$

5. Conditions and closure

Again, we treat the straight wall first (Fig. 1) and concentrate on the corners afterward (Figs. 2 and 3). In general, the symmetry of the problem should be reflected in the closure formulation. For a straight wall the symmetry axis is the normal, defined by links 4 and 8, and for the corners it is the line defined by links 3 and 7.

6. Straight wall

After streaming over the whole domain the populations f_3, f_4, and f_5 are incoming populations from the fluid. The populations f_0, f_2, and f_6 come from boundary nodes, whereas f_1, f_7, and f_8 are the unknown outgoing populations and should be chosen in order to satisfy the desired boundary condition. They are responsible for transmitting the effect of the wall to the fluid. In addition, the density on the boundary node ρ^{wall} is unknown. Similar to [6,18], we list the constraints for f_i^{neq} at the boundary node arising from the collision invariance of density [Eq. (2.12)] from the collision invariance of momentum [Eq. (2.13)] and from Eq. (2.17) using the results of Sec. IV A and where we have replaced $f_i^{(1)}$ by f_i^{neq}. After effecting a few algebraic manipulations, we obtain the following algebraic system:

$$f_1^{neq} + f_2^{neq} + f_3^{neq} = 0, \tag{4.28}$$

$$f_5^{neq} + f_6^{neq} + f_7^{neq} = 0, \tag{4.29}$$

$$f_1^{neq} + f_8^{neq} + f_7^{neq} = 0, \tag{4.30}$$

$$f_3^{neq} + f_4^{neq} + f_5^{neq} = 0, \tag{4.31}$$

$$f_0^{neq} + f_2^{neq} + f_6^{neq} = 0, \tag{4.32}$$

$$f_2^{neq} - f_4^{neq} + f_6^{neq} - f_8^{neq} = 0, \tag{4.33}$$

$$-f_1^{neq} + f_3^{neq} - f_5^{neq} + f_7^{neq} = -\frac{2c_s^2\rho}{\omega} S_{xy}. \tag{4.34}$$

For a straight wall the off-diagonal component of the rate of strain tensor S_{xy} is generally an unknown so that we remove Eq. (4.34) from the list and only use Eqs. (4.28)–(4.33) to derive a closure for the unknown populations.

We will regard all populations, not only f_1, f_7, and f_8, as unknowns. Given that the number of equations is smaller than the number of unknowns, our first question is for which unknowns do we solve the system of equations and which unknowns do we take as initially given. Considering the geometry of the problem, it is natural to suppose $f_i^{in} = f_i^{ps}$, $i = 3,4,5$, since these populations are coming from nodes where a usual BGK collision took place and carried useful information. Therefore we remove them directly from the list of unknowns. Nevertheless, for some cases it might be necessary to modify also the populations streamed in from bulk-fluid nodes, for instance, at corners, as we will see below. The populations f_0^{ps}, f_2^{ps}, and f_6^{ps} are coming from boundary nodes where populations have been artificially modified before collision and might therefore transport erroneous information, as will be shown in Sec. V A. In order to determine the density on the boundary node ρ^{wall}, we have to adopt one of the two mass conservation formulas. We opt for the fluid perspective of Chopard and Dupuis for reasons which will soon become clear. At the boundary node the equilibrium part of the populations has the following simple form:

$$f_i^{eq} = t_i \rho^{wall}. \tag{4.35}$$

Using this fact and Eq. (4.30) the mass conservation condition [Eq. (4.15)] leads to

$$m^{ps} = f_3^{in} + f_4^{in} + f_5^{in} \tag{4.36}$$

$$= m^{out} \tag{4.37}$$

$$= (1-\omega)(f_1^{neq} + f_8^{neq} + f_7^{neq}) + (f_1^{eq} + f_8^{eq} + f_7^{eq}) \tag{4.38}$$

$$= (f_1^{eq} + f_8^{eq} + f_7^{eq}) \tag{4.39}$$

$$= \tfrac{1}{6}\rho^{wall}. \tag{4.40}$$

Therefore we have a definition for the density at the wall,

$$\rho^{wall} = 6m^{ps}. \tag{4.41}$$

This leads immediately to

$$f_3^{in} + f_4^{in} + f_5^{in} = f_3^{eq} + f_4^{eq} + f_5^{eq} \tag{4.42}$$

$$+ f_3^{neq} + f_4^{neq} + f_5^{neq} \tag{4.43}$$

$$= f_3^{eq} + f_4^{eq} + f_5^{eq}. \tag{4.44}$$

Thus, Eq. (4.31) is respected by mass conservation. If we had adopted the boundary-fluid perspective of Hollis *et al.*, then Eq. (4.31) would not have been automatically satisfied and we would have to keep one of the populations coming from bulk-fluid nodes as variable in order to respect condition (4.31).

Another way of defining ρ^{wall} is to require that condition (4.31) should hold true [which follows from Eqs. (2.13) and (4.2)] and which translates to

$$f_3^{in} + f_4^{in} + f_5^{in} = f_3^{eq} + f_4^{eq} + f_5^{eq} \tag{4.45}$$

$$= \tfrac{1}{6}\rho^{wall}. \tag{4.46}$$

Finally, together with Eq. (4.30), we obtain a mass conserving boundary condition in the fluid perspective. Thus conditions (2.13) and (4.2) lead to conservation of mass [Eq. (4.15)]. Since Eq. (4.31) is now satisfied by the choice of ρ^{wall}, we can remove it from our list of conditions. The nonequilibrium parts f_3^{neq}, f_4^{neq}, and f_5^{neq} are now given and lead to the remaining set of conditions,

$$f_1^{neq} + f_2^{neq} = -f_3^{neq}, \tag{4.47}$$

$$f_6^{neq} + f_7^{neq} = -f_5^{neq}, \tag{4.48}$$

$$f_1^{neq} + f_8^{neq} + f_7^{neq} = 0, \tag{4.49}$$

$$f_0^{neq} + f_2^{neq} + f_6^{neq} = 0, \tag{4.50}$$

$$f_2^{neq} + f_6^{neq} - f_8^{neq} = f_4^{neq}, \tag{4.51}$$

for the unknowns f_i^{neq}, $i = 0,1,2,6,7,8$. We are now left with two possibilities: we could either move f_0^{neq} to the right-hand

side, which means take it as an input parameter, or either f_2^{neq} and f_6^{neq}. Equation (4.50) does not allow us to choose f_0^{neq}, f_2^{neq}, and f_6^{neq} as input parameters at the same time.

(1) *Choosing* f_2^{neq} and f_6^{neq} as input. If we consider in a first moment only Eqs. (4.47), (4.48), (4.50), and (4.51) and take $f_2^{in}=f_2^{ps}$ and $f_6^{in}=f_6^{ps}$, that means f_2^{neq} and f_6^{neq} are now initially given, we obtain for the unknowns f_i^{neq}, $i=0,1,7,8$ the following solution:

$$f_1^{neq} = -f_2^{neq} - f_3^{neq}, \tag{4.52}$$

$$f_7^{neq} = -f_6^{neq} - f_5^{neq}, \tag{4.53}$$

$$f_8^{neq} = -f_4^{neq} + f_2^{neq} + f_6^{neq}, \tag{4.54}$$

$$f_0^{neq} = -f_2^{neq} - f_6^{neq}, \tag{4.55}$$

and we verify that this solution satisfies Eq. (4.49). If we add one half times Eq. (4.31) to f_1^{neq} and f_7^{neq} we obtain the more pertinent form,

$$f_1^{neq} = \tfrac{1}{2}f_4^{neq} + \tfrac{1}{2}(f_5^{neq} - f_3^{neq} - 2f_2^{neq}), \tag{4.56}$$

$$f_7^{neq} = \tfrac{1}{2}f_4^{neq} - \tfrac{1}{2}(f_5^{neq} - f_3^{neq} + 2f_6^{neq}), \tag{4.57}$$

$$f_8^{neq} = -f_4^{neq} + f_2^{neq} + f_6^{neq}, \tag{4.58}$$

$$f_0^{neq} = -f_2^{neq} - f_6^{neq}. \tag{4.59}$$

We will call this closure "no-slip A" boundary condition. So far we have not used any further assumptions.

If, instead of taking f_2^{neq} and f_6^{neq} initially given, we insert the result suggested by the Chapman-Enskog expansion and the hydrodynamic implications [Eq. (4.7)] for f_i^{neq}, $i=2,6$, i.e., we set $f_2^{neq}=f_6^{neq}=0$, we obtain the following boundary condition:

$$f_1^{neq} = \tfrac{1}{2}f_4^{neq} + \tfrac{1}{2}(f_5^{neq} - f_3^{neq}), \tag{4.60}$$

$$f_7^{neq} = \tfrac{1}{2}f_4^{neq} - \tfrac{1}{2}(f_5^{neq} - f_3^{neq}), \tag{4.61}$$

$$f_8^{neq} = -f_4^{neq}. \tag{4.62}$$

In the following, this closure will be referred to as the "no-slip B" boundary condition.

(2) *Choosing* f_0^{neq} as input. In this case Eq. (4.50) will simply change to

$$f_2^{neq} + f_6^{neq} = -f_0^{neq}. \tag{4.63}$$

If we now consider choosing the leading term for f_0^{neq} as its value, i.e., setting f_0^{neq} to zero [Eq. (4.7)], we end up with

$$f_2^{neq} = -f_6^{neq}, \tag{4.64}$$

which states that the nonequilibrium parts of the tangential populations are antisymmetric. Using this result, we obtain the following set of equations:

$$f_2^{neq} + f_6^{neq} = 0, \tag{4.65}$$

$$f_1^{neq} + \tfrac{1}{2}(f_2^{neq} - f_6^{neq}) = -f_3^{neq}, \tag{4.66}$$

$$f_7^{neq} - \tfrac{1}{2}(f_2^{neq} - f_6^{neq}) = -f_5^{neq}, \tag{4.67}$$

$$f_8^{neq} = -f_4^{neq}, \tag{4.68}$$

from which follows that also the nonequilibrium parts of the normal populations are antisymmetric. We verify that the unused condition (4.49) is satisfied. Since we have five unknowns on the left-hand side, but only four equations, the space of unknowns can be described by one parameter. In line with the symmetry of the problem we define this parameter to be $\Delta f=f_2^{neq}-f_6^{neq}$. Adding one half times Eq. (4.31) to the second and third equations [Eqs. (4.66) and (4.67)], we obtain the more pertinent form,

$$f_2^{neq} = \frac{\Delta f}{2}, \tag{4.69}$$

$$f_6^{neq} = -\frac{\Delta f}{2}, \tag{4.70}$$

$$f_1^{neq} = \tfrac{1}{2}f_4^{neq} + \tfrac{1}{2}(f_5^{neq} - f_3^{neq} - \Delta f), \tag{4.71}$$

$$f_7^{neq} = \tfrac{1}{2}f_4^{neq} - \tfrac{1}{2}(f_5^{neq} - f_3^{neq} - \Delta f), \tag{4.72}$$

$$f_8^{neq} = -f_4^{neq}, \tag{4.73}$$

$$f_0^{neq} = 0. \tag{4.74}$$

Once we find a suitable value for Δf we have closed the system of equations. A possible closure for Δf could, for instance, be the value obtained by inserting the leading terms for f_2^{neq} and f_6^{neq} which leads to $\Delta f=0$ and we end up with the no-slip B closure. Therefore, we define Δf to be the value after streaming,

$$\Delta f = \frac{f_2^{ps} - f_6^{ps}}{2}. \tag{4.75}$$

The boundary condition corresponding to this choice will be called "no-slip C" boundary condition.

During our derivation we end up with the following surprising result for the no-slip C boundary condition:

$$f_2^{neq} = -f_6^{neq} \text{ and } f_4^{neq} = -f_8^{neq}, \tag{4.76}$$

which seems to contradict Eq. (2.14) stating that the leading order term of the nonequilibrium parts of the populations aligned with the grid axes should be symmetric in $\vec{c}_i$. Nevertheless at the no-slip boundary we know from Sec. IV B that the leading order term is identical to zero since we have chosen the Mach number sufficiently small. Thus there is no apparent reason for choosing f_8^{neq} symmetric or antisymmetric to f_4^{neq}. An analysis of the subhydrodynamic scales at the boundary, i.e., performing a multiscale analysis up to higher than second order, is beyond the scope of the present discussion. However an analogon can be found. It is interesting to note that the explicit form of the equilibrium distribution at the boundary [formula (4.35)] corresponds to the equilibrium distribution function for a diffusive lattice Boltzmann method [3,14,20]. For this kind of lattice Boltzmann methods

we know that the leading term of the nonequilibrium part is proportional to $t_i\vec{c}_i\cdot\nabla\rho$, thus antisymmetric. Therefore it is reasonable to construct the nonequilibrium parts of the populations aligned with the grid axes in analogy to a diffusive lattice Boltzmann method since it would also correspond to the different physical regimes we observe at the interior of the flow and at the boundary, mentioned in Sec. IV A. These considerations explain also the seemingly *ad hoc* introduction of the leading term for f_0^{neq} when deriving the no-slip C boundary condition. Indeed, if we had required $f_2^{neq}=-f_6^{neq}$, we would have obtained $f_0^{neq}=0$ by Eq. (4.50).

We remark that we derived our closures starting from the condition of collision invariance of density and momentum and basic implications about the rate of strain tensor at the boundary to obtain the system [Eqs. (4.28)–(4.33)]. Second, we chose three incoming populations we assumed to contain most relevant information. We checked that the definition of the density at the wall ρ^{wall} obtained by mass conservation does not contradict the system of equations. This lead us to a system of five equations [Eqs. (4.47)–(4.51)] for six unknowns f_i^{neq}, $i=0,1,2,6,7,8$. Finally, we formulated different closure possibilities among which the no-slip A and no-slip C boundary conditions use information from tangential populations whereas the no-slip B boundary condition relies only on information from bulk-fluid nodes.

7. External corner

For this case, the off-diagonal component of the rate of strain tensor is known, $S_{xy}=0$, therefore Eqs. (4.28)–(4.34) have to be fulfilled. We can immediately see that we cannot take the nonequilibrium part of all populations coming from bulk-fluid nodes as initially given since this would lead to contradictions. The Chopard-Dupuis mass conservation condition states the following:

$$m^{ps}=\sum_{i=1,2,3,4,5} f_i^{ps} \tag{4.77}$$

$$=m^{out} \tag{4.78}$$

$$=(1-\omega)\sum_{i=1,5,6,7,8} f_i^{neq}+\sum_{i=1,5,6,7,8} f_i^{eq} \tag{4.79}$$

$$=-(1-\omega)f_7^{neq}+\tfrac{11}{36}\rho^{wall}, \tag{4.80}$$

where we have used Eqs. (4.28) and (4.29). In order to obtain a simple expression for the density at the corner node we can choose $f_7^{neq}=0$ as an additional constraint. We check that this is compatible with the Chapman-Enskog expansion [Eq. (4.9)]. Choosing additionally f_2^{neq} and f_4^{neq} as initially given, we obtain the following closure:

$$f_0^{neq}=-\tfrac{2}{3}f_2^{neq}-\tfrac{2}{3}f_4^{neq}, \tag{4.81}$$

$$f_1^{neq}=-\tfrac{2}{3}f_2^{neq}+\tfrac{1}{3}f_4^{neq}, \tag{4.82}$$

$$f_3^{neq}=-\tfrac{1}{3}f_2^{neq}-\tfrac{1}{3}f_4^{neq}, \tag{4.83}$$

$$f_5^{neq}=\tfrac{1}{3}f_2^{neq}-\tfrac{2}{3}f_4^{neq}, \tag{4.84}$$

$$f_6^{neq}=-\tfrac{1}{3}f_2^{neq}+\tfrac{2}{3}f_4^{neq}, \tag{4.85}$$

$$f_8^{neq}=\tfrac{2}{3}f_2^{neq}-\tfrac{1}{3}f_4^{neq}. \tag{4.86}$$

And the density is given by

$$\rho^{wall}=\tfrac{36}{11}m^{ps}.$$

We remark that it is also possible to keep f_3^{neq} as initially given instead of choosing $f_7^{neq}=0$. However, the definition of the density at the wall would be more involved,

$$\rho^{wall}=\tfrac{36}{11}\frac{1}{\omega}[m^{ps}-(1-\omega)(f_2^{in}+f_4^{in}+3f_3^{in})].$$

Therefore we use the first version as the present corner formulation. Other formulations are definitely possible, for example, choosing f_1^{neq} and f_5^{neq} as initially given, but we stick to the present one since it seems to be the most stable and accurate one during the tests we performed beforehand.

8. Internal corner

As for the external corner the off-diagonal component of the rate of strain tensor is known, $S_{xy}=0$. For the internal corner the mass conservation formulation of Chopard and Dupuis reads

$$m^{ps}=f_3^{ps} \tag{4.87}$$

$$=(1-\omega)f_7^{neq}+f_7^{eq} \tag{4.88}$$

$$=(1-\omega)f_7^{neq}+\tfrac{1}{36}\rho^{wall}. \tag{4.89}$$

Thus, similar to the external corner, choosing $f_7^{neq}=0$ as an additional constraint leads to

$$\rho^{wall}=36m^{ps}.$$

If we keep $f_3^{in}=f_3^{ps}$ and set $f_1^{neq}=f_5^{neq}=0$ (since these do not play a role), we get for the internal corner

$$f_i^{neq}=0,\quad i=0,\ldots,8.$$

V. NUMERICAL VERIFICATION

The numerical verification is done in four parts by four different benchmark tests with increasing complexity: steady Poiseuille flow (Sec. V C), unsteady Womersley flow (Sec. V D), steady flow over a backward facing step (Sec. V E), and unsteady flow around a square cylinder (Sec. V F). Before going over to these benchmark tests we have a glance at numerical stability (Sec. V A) and the definition of the numerical error (Sec. V B).

A. Stability

If numerical instabilities occur in numerical simulations, they often originate at the boundaries. Therefore, stability of

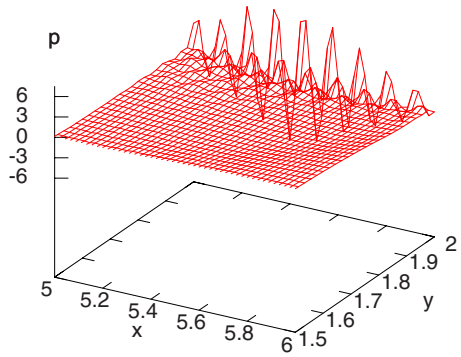

FIG. 4. (Color online) Numerical wave-type instability of the pressure field p arising from the no-slip C condition at the boundary situated at $y=2$. This type of instability grows with simulation time and will finally spread over to the whole computational domain.

boundary conditions is a crucial issue in computational fluid dynamics.

While using the no-slip A and the no-slip C boundary conditions, we observed the development of perturbations in the density (pressure) field along the boundary with a wavelength of the order of δx for a relaxation frequency $\omega \gtrapprox 1.5$ ($\omega \gtrapprox 1.8$) (see Fig. 4). The fact that these perturbations travel along the boundary indicates that they are induced by the tangential populations. Indeed, using the no-slip B boundary condition which does not use information from the boundary nodes, these high wave number perturbations are absent in the pressure field. As we will see in Sec. V B, the drawback of doing so is a slight reduction in accuracy. Nevertheless the immense gain in stability compensates this loss. Since the no-slip A boundary condition is unstable for relatively small values of ω, we continue our discussion only with the no-slip B and no-slip C boundary conditions.

B. Numerical error

The $\mathcal{L}_2$ norm of the error can be estimated by a power k of the grid size and a constant c. The power k is called the order of convergence because it indicates the order by which the error is reduced with grid refinement. For a steady flow system, the resolution is only spatial. In case of a lattice Boltzmann method the grid spacing, δx and δy, is uniform in both spatial directions; therefore the spatial resolution is only given by one parameter N, the number of sections into which the reference length is divided by the grid points,

$$\delta x = \delta y = \frac{1}{N}.$$

In this case, having a reference solution of the velocity $\vec{u}_{ref}$, we can define an error as follows:

$$\epsilon_N = \sqrt{\frac{1}{N_{err}} \sum_{\vec{x} \in N_{err}} |\vec{u}_{num}(\vec{x}) - \vec{u}_{ref}(\vec{x})|^2} \leq c \frac{1}{N^k}, \quad (5.1)$$

where N_{err} is the ensemble and/or number of points of the entire domain. The respective error on the pressure field is defined in a similar way. When dealing with a section we use the $\mathcal{L}_1$ error,

$$\epsilon_N = \frac{1}{N_{err}} \sum_{\vec{x} \in N_{err}} |\phi_{num}(\vec{x}) - \phi_{ref}(\vec{x})|, \quad (5.2)$$

where N_{err} is the ensemble and/or number of points of the section and ϕ is either u, v, or p.

The grid refinement is done by keeping the viscosity constant, that is, we choose the time step δt to be proportional to the square of the grid spacing δx,

$$\delta t \propto \delta x^2 = \frac{1}{N^2}. \quad (5.3)$$

In this way, the compressibility error is also reduced with second-order accuracy since it scales with the square of the Mach number. The Mach number itself scales with $\delta t / \delta x$.

C. Numerical verification (part 1)

In this section we investigated the accuracy of the present boundary condition on the basis of a laminar Poiseuille flow.

1. Poiseuille flow

We start the numerical analysis of the boundary conditions for the lattice Boltzmann method by the help of a concrete example, namely, Poiseuille flow in two dimensions. This type of flow can either be pressure driven or driven by a body force. In contrary to numerical methods solving the Navier-Stokes equations for which pressure gradient and body force can be merged together, a lattice Boltzmann method introduces these two effects differently. Since a body force will introduce additional inaccuracies [21], we made only use of pressure driven flow. We placed our coordinate system in such a way that the x axis is along the channel walls and the y axis is perpendicular to the walls. As inflow condition we used a velocity inlet with an analytical Poiseuille profile. At the outlet the pressure was kept constant. Poiseuille flow has an analytical velocity profile given by

$$u_x^* = u^*(y^*) = 4y^*(1-y^*) \text{ and } u_y^* = v^* = 0,$$

where the asterisk stands for dimensionless quantities in terms of a reference velocity (here the maximum velocity in the channel center u_{max}) and a reference length (here the channel width d). The pressure gradient can also be made dimensionless [$p^* = p/(\rho u_{max}^2)$],

$$\frac{\partial p^*}{\partial x^*} = -\frac{8}{\mathrm{Re}},$$

where $\mathrm{Re} = u_{max} d / \nu$ is the Reynolds number of the flow.

2. Numerical results

We computed a Poiseuille flow performing subsequent grid refinements to verify the accuracy of different types of boundary conditions for different values of the relaxation frequency ω. Figures 5 and 6 display the error as a function of the resolution N. Since the time step was decreased according to Eq. (5.3) the total number of time steps needed to reach steady state varies from resolution to resolution. For the present case we needed, independent of the boundary

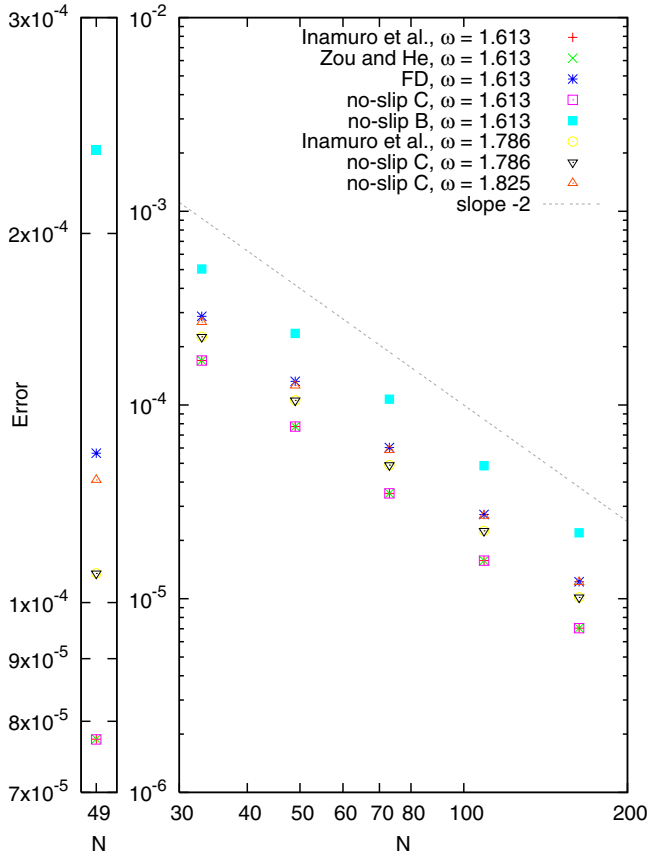

FIG. 5. (Color online) Right: error scaling of the velocity field for different boundary conditions for Poiseuille flow for $1.613 \leq \omega \leq 1.825$ ($10 \leq \mathrm{Re} \leq 25$). We remark that the values for the no-slip C, the boundary conditions of Inamuro *et al.* and Zou and He, are so close together that they appear on the same spot. Left: detail for $N=49$.

condition used, around 7000 time steps for $N=33$ and up to 160 000 for $N=163$. As initial condition we imposed $\vec{u}=\vec{0}$ and $\rho=1$ inside the domain. The error was evaluated using formula (5.1). As inflow and outflow conditions we used, as already mentioned, the FD boundary conditions of Lätt *et al.* [4] presented in Sec. III.

At a value of $\omega \approx 1.8$ the simulation using the boundary conditions of Inamuro *et al.* [8] or Zou and He [12] became unstable corresponding to what Lätt *et al.* found in their analysis [4]. For a slightly higher value of ω, also the simulation with no-slip C boundary conditions became unstable. In contrast to this, the simulations with FD and no-slip B boundary conditions stayed stable until a value of $\omega \approx 1.99$ ($\omega \approx 1.995$). The fact that the no-slip B boundary condition stays stable up to a relatively high value for ω corresponds to what we expect from the discussion in Sec. V A. The reason for this is the suppression of the tangential populations and the resulting absence of growing instabilities along the boundaries. Concerning accuracy, our first statement is that all boundary conditions reveal second-order accuracy. Nevertheless, differences concerning the value of the coefficient c exist. The boundary condition of Inamuro *et al.* and Zou and He and the no-slip C boundary condition are found to be equally accurate, so that their marks appear on the same

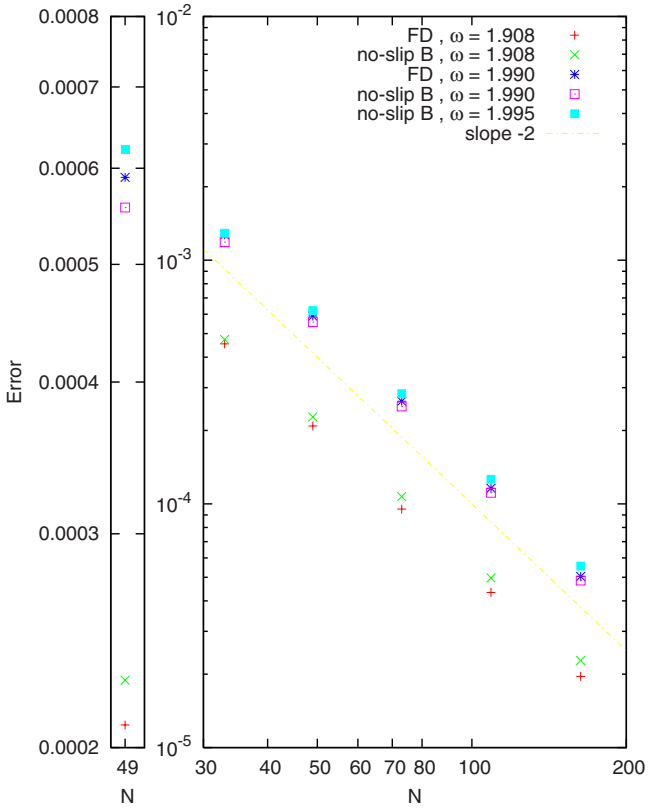

FIG. 6. (Color online) Right: error scaling of the velocity field for different boundary conditions for Poiseuille flow for $1.908 \leq \omega \leq 1.995$ ($50 \leq \mathrm{Re} \leq 1000$). Left: detail for $N=49$.

spots in Fig. 5. We definitely can conclude that the FD and no-slip B boundary condition are less accurate but more stable than the others and therefore more suitable to simulate high Reynolds number flows.

D. Numerical verification (part 2)

The foregoing benchmark test certified the second-order accuracy of the present boundary conditions for a steady flow simulation. In this section we verified the accuracy for an unsteady flow simulation. Due to its simplicity, Womersley flow was chosen.

1. Womersley flow

The Womersley flow [22] is an unsteady time-periodic variant of Poiseuille flow. The flow is aligned with the channel walls (x axis) and only a function of the normal (y axis) and time, such that the convective terms become zero. The pressure gradient is no longer constant but oscillates with a frequency $f^*=fd/u_{max}$,

$$\frac{\partial p^*}{\partial x^*} = -\mathrm{Re}\left(\frac{8}{\mathrm{Re}}\exp(if^*t^*)\right),$$

where Re is the real part. The oscillation introduces a dimensionless number: the Womersley number,

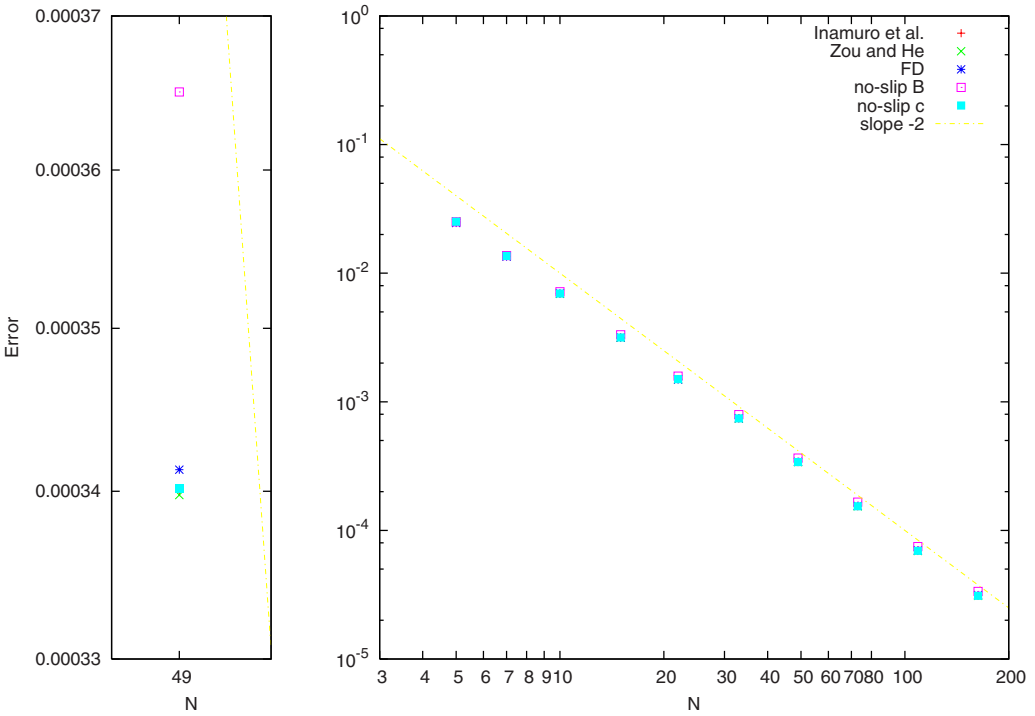

FIG. 7. (Color online) Right: error scaling of the velocity field for different boundary conditions for Womersley flow for $\omega=1.613$ (Re=10, $\alpha=5$). Left: detail for $N=49$.

$$\alpha = \sqrt{\frac{\mathrm{Re}\, f^*}{4}}.$$

For this flow we can find an analytical velocity profile given by

$$u^*(t^*,y^*) = \mathrm{Re}\left(-\frac{8}{i\,\mathrm{Re}\, f^*}\exp(if^*t^*)\left\{1 - \frac{\cosh[\sqrt{2}(y^*-1/2)(\alpha+i\alpha)]}{\cosh[(\alpha+i\alpha)/\sqrt{2}]}\right\}\right),$$

where Re refers to the real part.

2. Numerical results

Figure 7 demonstrates the similarity in accuracy of the boundary condition of Inamuro *et al.* and Zou and He and the no-slip C boundary condition. The no-slip B boundary condition is also second-order accurate but with a larger coefficient. These results confirm the results of Sec. V D 1 for the unsteady case.

E. Numerical verification (part 3)

The foregoing benchmark tests showed that the present boundary conditions can simulate a velocity profile correctly and do not deteriorate the order of convergence of the lattice Boltzmann method. Nevertheless, more severe benchmark tests are necessary in which the convective terms play a dominant role and more complex boundary layer phenomena such as separation and reattachment appear. Precisely for these reasons, the backward facing step flow was chosen as our third benchmark test.

1. Backward facing step flow

The backward facing step flow is a popular benchmark test for numerical codes [23] for laminar as well as for turbulent flows. In the present discussion we consider the laminar case, where the setup consist of a velocity inlet with a Poiseuille velocity profile. Depending on the Reynolds number, the flow will give rise to one or more recirculation zones (cf. Fig. 8). The flow leaves the computational domain with a Poiseuille profile again. The ratio of the step height to the inlet section is one in our case. The reference length is based on one half of the inlet height h and the reference speed on the average velocity at the inlet.

The case having received most attention is the case at Re=800. This test case has been computed by a number of methods, so that we can rely on data in the literature to compare our numerical solutions. More precisely, we chose the solutions of Gartling [24] and Erturk [25] as a reference to our simulation. Gartling used a Galerkin-based finite element method to solve the steady Navier-Stokes equations, whereas Erturk employed a second-order finite difference

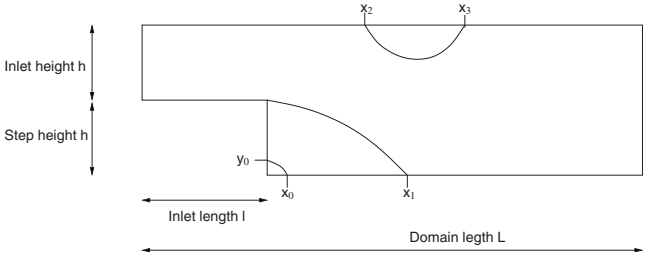

FIG. 8. Geometry of the backward facing step.

TABLE II. Details of the geometry and the grids used.

	l/h	L/h	$\delta x/h$	$\delta y/h$
Gartling	0	60	0.025	0.025
Erturk	20	320	0.04	0.02
Present	5	70	0.017	0.017

method solving the steady Navier-Stokes equations in stream function vorticity formulation. Details about the geometry are outlined in Table II. We mention that Gartling used a slightly different geometry by placing the inlet directly at the step. The resolution in y direction used for the simulations is increasing from Gartling's over Erturk's to the present case. Erturk used a different resolution in x whereas Gartling's mesh is squared in the domain next to the step. A necessary condition for LBGK is that the lattice is equally spaced in both directions, so that we did not have any other choice than using the same resolution along x.

There are multiple interesting features to check the accuracy of the numerical solution. The ones we were focusing on are the following:

(i) pressure and velocity profiles at the distances $x/h=6,14,30$ from the step,

(ii) positions of separation and reattachment points, and

(iii) positions of the center of the eddies and the values of the stream function and the vorticity at these points.

We renounce to give profiles for the vorticity and the first derivatives of the velocity since their accuracy depends on the finite difference scheme used to postprocess the velocity fields but do not give any new insights into the actual accuracy of the numerical method. This is also the reason why we do not present contour plots of the whole domain, but we restrict ourselves to selected profiles allowing a detailed comparison of the accuracy.

Before tackling the Re=800 case we checked the accuracy of the velocity and pressure field for the Re=66 case which has a relaxation frequency, $\omega=1.748$, sufficiently low to allow comparisons with the other boundary conditions tested before.

2. Numerical results

A first convergence check for the above considered boundary conditions (cf. Fig. 9) revealed a similar behavior of the error of the numerical simulation to a reference solution [formula (5.1)] for all boundary conditions. This is what we expected since all numerical experiments start from the same initial conditions, $\vec{u}=0$ and $\rho=1$, for all points in the computational domain. Only when approaching the steady state solution, we saw differences appearing concerning the steady state value of the error. The overall behavior is an oscillatory evolution toward a steady state. It is interesting to remark that the pressure field tends to approach the steady state more slowly than the velocity field. Therefore, a convergence check both of the velocity field and of the pressure field is needed in order to determine the steady state. The reference solution is an accurate simulation with a resolution of $N=120$ or a grid spacing of $\delta x=0.0083$ using no-slip B boundary conditions. This reference solution was then used to create the error plot (Fig. 10). Before we go over to the

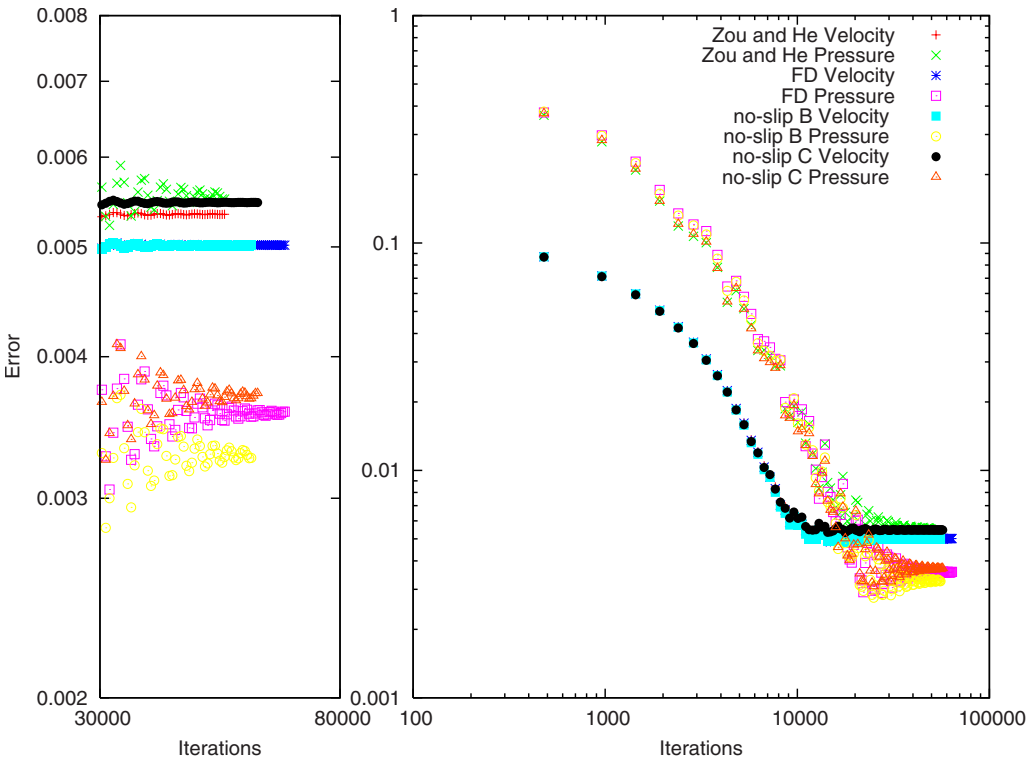

FIG. 9. (Color online) Right: behavior of the error of the velocity and pressure field for the backward facing step for different boundary conditions, $N=24$, Re=66. Left: detail of the approach of the steady state value.

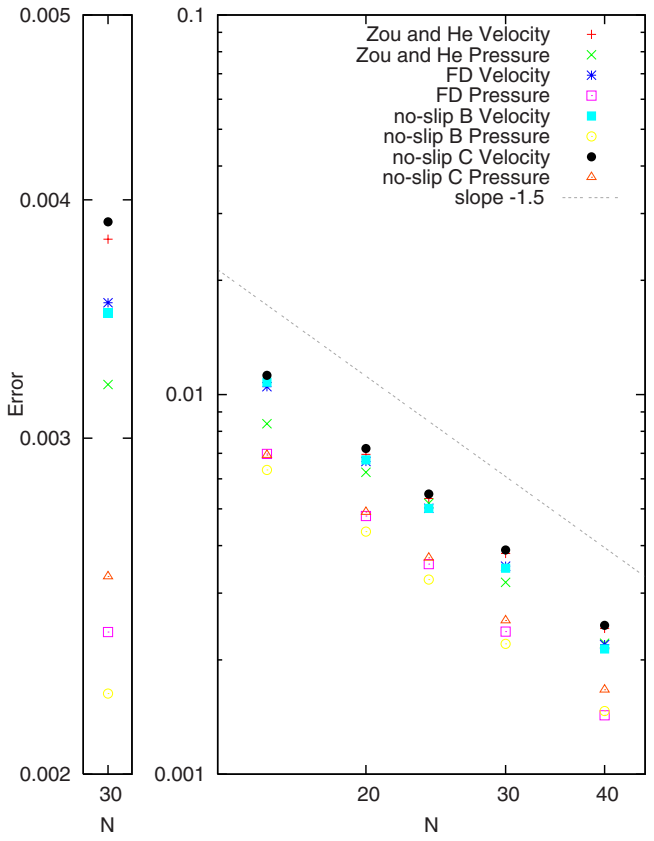

FIG. 10. (Color online) Right: error scaling of the velocity and pressure field for the backward facing step for different boundary conditions, Re=66. Left: detail for $N=30$.

discussion of this plot, we mention that we checked whether the position of the points on this plot depends on the boundary condition used for computing the reference solution. Therefore we used a reference solution computed with no-slip C boundary conditions, performing worst for this case, to create a second plot, but we did not find any difference to the plot created with no-slip B boundary conditions. This confirms that the reference solution is accurate enough to allow such a convergence test. Concerning the order of convergence, we are faced with a different picture than in the case of Poiseuille and Womersley flows (cf. Fig. 10). The order of convergence is rather 1.5 than 2, independent of the boundary condition used. High gradients at the step corner cause problems and lead to spurious oscillations in the pressure field when using a nonstaggered grid. This has been observed for, among others, finite difference schemes [23], finite element methods [24], and spectral domain decomposition methods [26]. The lattice Boltzmann method is also concerned by this problem and no matter what corner formulation is used, either the generic corner formulation of Lätt *et al.* (Sec. III) or the present one (Sec. IV), the pressure field around the step shows spurious oscillations (see Figs. 11 and 12). Therefore, the flow around the step corner is difficult to resolve and introduces spurious oscillations in the pressure field. In order to verify whether the deterioration of the convergence rate is due to the spurious oscillations at the step corner or not, we performed a convergence test based only on the eastern half of the computational domain, two h from the step away (see Fig. 13). As expected the convergence is again of second order. Returning to Fig. 10, it is interesting to note that the most accurate boundary conditions for Poiseuille flow are performing worse than the less accurate boundary conditions, the FD and the no-slip B boundary conditions, although the difference is marginal. A reason for

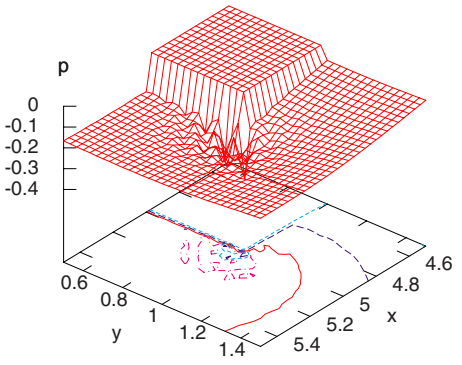

FIG. 11. (Color online) Spurious oscillations in the pressure field p at the step corner of the backward facing step flow. The plane $p=0$ marks the step. The oscillations do not spread out but stay locally at the step corner. For this figure the generic corner formulation of Lätt *et al.* [4,15] has been used.

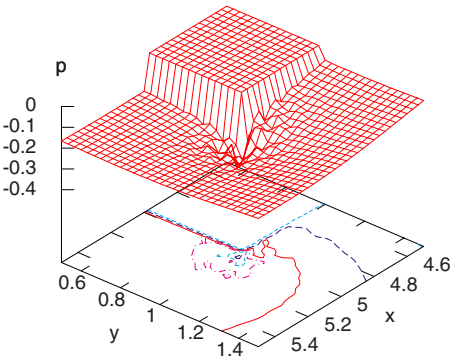

FIG. 12. (Color online) The same as in Fig. 11, but this time the present corner formulation, cf. Sec. IV, has been used. The spurious oscillations do arise no matter what kind of corner formulation used.

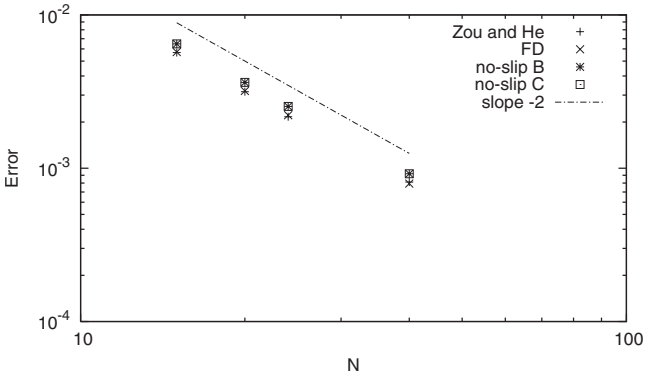

FIG. 13. Error scaling of the velocity field for the backward facing step for different boundary conditions for a domain excluding the step corner, Re=66.

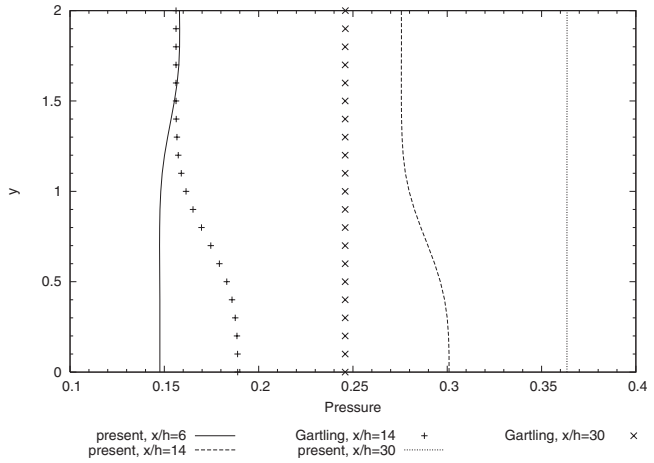

FIG. 14. Pressure profiles at $x/h=6$, $x/h=14$ and $x/h=30$.

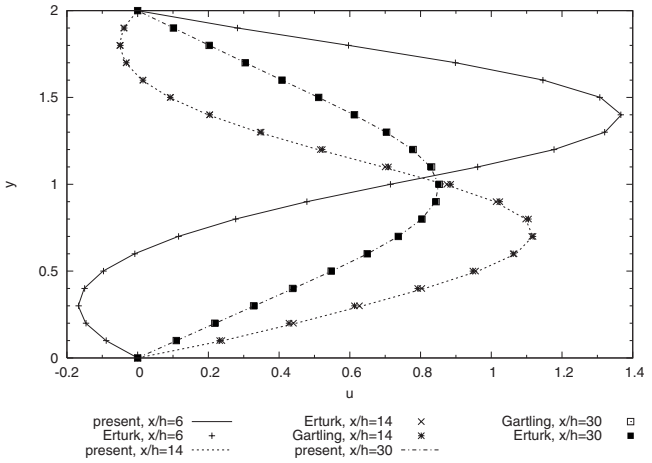

FIG. 16. u profiles at $x/h=6$, $x/h=14$ and $x/h=30$.

this deterioration of accuracy might be due to a less efficient damping of the tangential instabilities, discussed in Sec. V A. Since the FD and the no-slip B boundary condition do not use the tangential populations, they are not affected by these instabilities. The pressure field is less accurately resolved by the boundary condition of Zou and He than by the other three. Generally speaking, it seems that the FD and the no-slip B boundary conditions are performing better for this benchmark test, where spurious oscillations corrupt the solution in parts of the computational domain.

The no-slip B boundary condition was then used for the Re=800 case. A Reynolds number of 800 corresponds in our case to a relaxation frequency of $\omega=1.976$. Tables VIII–X display the details of the results for u, v, and p in comparison to the results of Gartling [24] and Erturk [25]. Since the pressure field next to the step corner is corrupted by spurious oscillations, the pressure constant determined by equating the value of the pressure at the step corner to zero is obviously wrong, as can easily be seen form Fig. 14. Therefore we determine a second pressure constant by equating the present pressure field to the pressure field of Gartling's simulation at position (14,2). This was an arbitrary choice without any intention to specially fit our result to the reference solution. The pressure profiles are displayed in Fig. 15. For this choice of the pressure constant we have errors $\epsilon=0.0029$ at $x/h=14$ and $\epsilon=0.0019$ at $x/h=30$ instead of 0.1166 and 0.1176 to Gartling's solution, shown in Table IX (Table X). The slightly different shape of the pressure profile for $x=14$ might have its origin in the fact that Gartling placed his inlet directly at the step corner. Unfortunately, Erturk does not provide any information about the pressure field of his solution. The present results for the velocity field, however, seem to match better Erturk's solution than Gartling's, although the correspondence to both solutions is fairly good. The average error [formula (5.2)] of u is for all velocity profiles compared to Erturk's solution around 10^{-4}–10^{-3} whereas it is, compared to Gartling's solution, around one order of magnitude larger (cf. Fig. 16 and Tables VIII–X). The y component of the velocity, v, matches the solution of Erturk and Gartling with a similar accuracy. There is, however, a discrepancy for the $x/h=14$ section, first mentioned by Erturk (see Fig. 17 and Table IX). Qualitatively, the present simulation agrees better with Erturk's than with Gartling's solution. A reason for this discrepancy might, as already mentioned, lie in the different geometries used by Gartling and the resolution of the grid. Thus the grid independent solution of the v profile at $x/h=14$ remains an open issue.

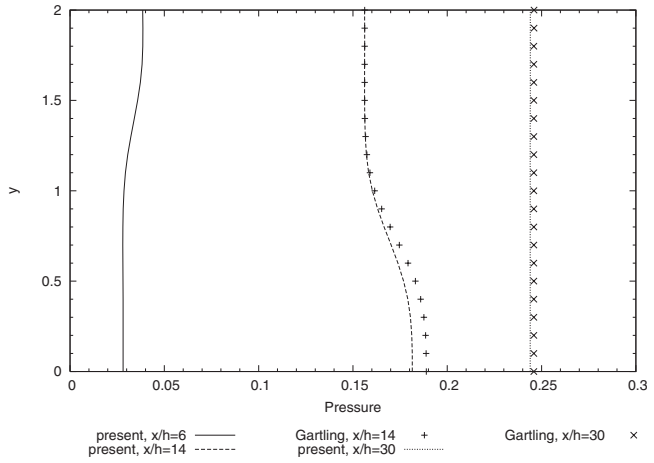

FIG. 15. Pressure profiles at $x/h=6$, $x/h=14$ and $x/h=30$ for an adapted pressure constant.

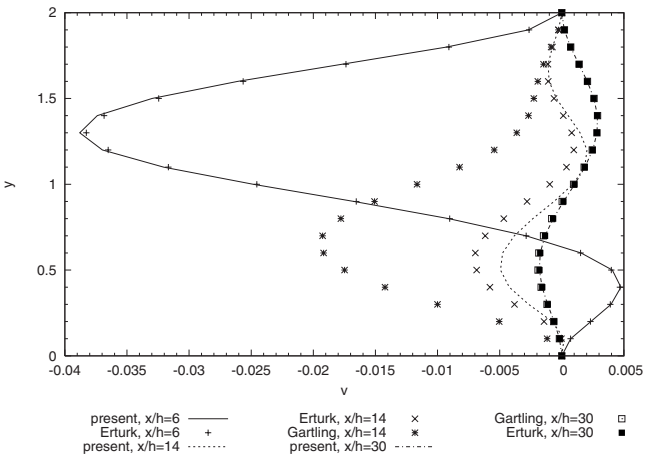

FIG. 17. v profiles at $x/h=6$, $x/h=14$ and $x/h=30$.

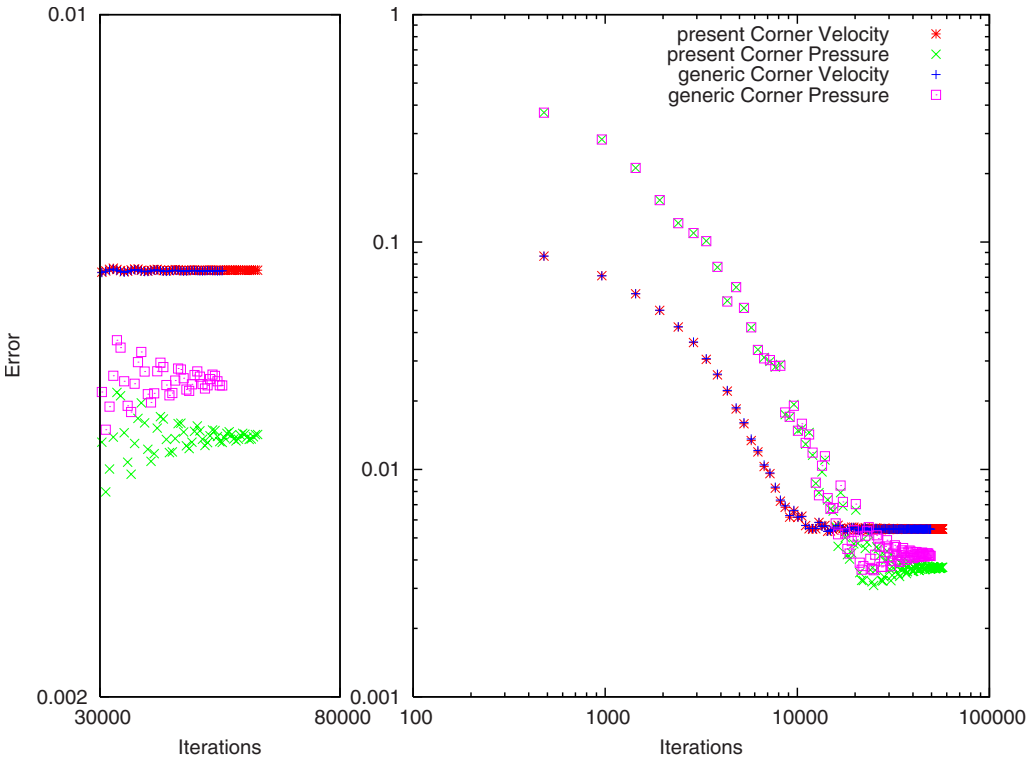

FIG. 18. (Color online) Right: Behavior of the error for two different kind of step corner formulations for the backward facing step for no-slip C boundary conditions, $N=24$, Re=66. Left: Detail of the approach of the steady state value.

As already mentioned, the step corner introduces oscillations in the pressure field. To investigate the dependence of these oscillations on the corner formulation, we tested the present corner formulation and the generic one. We set up a test case using the same boundary conditions but different corner formulations. As straight boundary condition we used the no-slip C condition. The Reynolds number is fixed at 66. From Figs. 11 and 12 we do not observe any fundamental difference in the spurious oscillations of the pressure field. This supports the statement that the causes of these oscillations are steep gradients appearing at the step corner. This evidence is also suggested by the fact that fundamentally different numerical schemes observe similar oscillations at the step corner. When looking at the behavior of the error of the two simulations (Fig. 18), there is no difference noticeable for the velocity field. The pressure field of the simulation, however, with the present corner, although not visible in Figs. 11 and 12, displays a slight increase in accuracy compared to the generic corner. In general, the impact of these oscillations is limited to a region close to the step corner.

Table III compares the values of the separation and reattachment lengths. These lengths are defined by the coordinates of the first grid point displaying a change in signs of u and v, respectively. Therefore, these values bear an error of the order of δx. Keeping this in mind, the results for the $x_2 - x_3$ eddy of the present simulation are surprisingly close to Erturk's result. For the reattachment length of the x_1 eddy, our result is different from Erturk's but still in the error margin. The spurious oscillations in the pressure field at the separation point, which is situated at the step corner, might play a role in this difference. Erturk did not solve the pressure field but instead used a ψ-ω formulation. Gartling's results instead show a larger discrepancy to Erturk's and ours, which again might be due to the different geometries of the computational domain. The smallest eddy $x_0 - y_0$, discovered by Erturk, is difficult to resolve but still in the error margin to Erturk's result. The computation for the eddy centers (cf. Table IV) involves a numerical differentiation and a numerical solution of a partial differential equation, as the vorticity ω has to be calculated from the velocity field, followed by the solution of a Poisson equation for the stream function ψ, thereby introducing additional numerical errors. Nevertheless, the present results are in good agreement to the reference simulations concerning positions and values of ψ and ω, apart from the upper $x_2 - x_3$ eddy, where the value of the

TABLE III. Position of the separation and reattachment points.

	x_0	y_0	x_1	x_2	x_3
Present	0.13	0.13	11.75	9.48	20.52
Erturk	0.154	0.138	11.834	9.476	20.553
Gartling			12.20	9.70	20.96

TABLE IV. Stream function and vorticity values at the eddy centers and their position.

		Eddy x_0-y_0	Eddy x_1	Eddy x_2-x_3
Present	ψ/ω	$1.93\times10^{-7}/0.0022$	$-0.034/-2.271$	0.507/1.208
	(x,y)	(0.07,0.05)	(6.62,0.59)	(14.53,1.63)
Erturk	ψ/ω	$8.04\times10^{-7}/0.0006$	$-0.0337/-2.262$	0.5065/1.092
	(x,y)	(0.08,0.06)	(6.68,0.58)	(14.60,1.64)
Gartling	ψ/ω		$-0.0342/-2.283$	0.5064/1.322
	(x,y)		(6.70,0.60)	(14.80,1.60)

vorticity differs the most. The value of ψ for the smallest eddy is resolved at the correct order of magnitude.

F. Numerical verification (part 4)

To conclude this section we performed a fourth verification, namely, time-periodic laminar flow around a square cylinder. We verified the present boundary condition by computing the Strouhal number, the mean drag coefficient and the root-mean-square value of the lift coefficient. This benchmark test is very complex since not only convective terms and different phenomena such as separation of flow play a dominant role but in addition the system is unsteady. In order to compare the no-slip B boundary condition to the bounce back rule, the latter one was also used to compute this test case. As already mentioned the bounce back rule has been intensively studied by different authors [5,7,8] and it has been emphasized that, for example, for a Poiseuille flow the position of the wall cannot be exactly located at the grid nodes which spoils the accuracy. However Inamuro *et al.* [8] showed that for ω close to 2, the bounce back rule becomes accurate again and therefore we expect similar results for the present no-slip B boundary condition and the bounce back rule.

1. Time-periodic laminar flow around a square cylinder

The geometry of this benchmark test consists of a square cylinder immersed in an infinite domain with the condition that the velocity should equal a constant velocity $\vec{u}=u\vec{e}_x$ at infinity, where we already defined the x axis of our coordinate system to be parallel to the free stream. The most frequently solved case in the literature is the one with a Reynolds number Re=100. The Reynolds number in this case is based on the free stream velocity u, the side length D of the square cylinder, and the kinematic viscosity of the fluid. For this Reynolds number the flow separates at the front edges of the cylinder [27] and a periodic shedding of vortices occurs behind the cylinder, the so-called Von Kármán vortex street. Again, we renounce to give contour plots of simulation results since these are not contributing to a better understanding of the numerical method.

This benchmark test poses two important numerical challenges. On the one hand, the representation of the infinite domain by a finite one requires the use of a large domain and/or boundary conditions on the artificial boundaries which reduce the influence of these on the simulation results. On the other hand, we have steep gradients in the domain next to the cylinder so that we need to have a good resolution in the vicinity of the cylinder. Therefore, it is advantageous to use a method allowing a nonuniform grid with a dense distribution of points next to the cylinder and a coarse distribution further away. An example of such a method is the finite difference method on a staggered grid used by Lankadasu and Vengadesan [28] to compute this test case. Since the standard lattice Boltzmann BGK method is only defined on equidistant Cartesian grids it is not well suited for this problem. Therefore, Cheng *et al.* [29] used a modified lattice Boltzmann method defined for nonuniform grids for this test case which is different from the standard lattice Boltzmann BGK method used throughout the present discussion. Robichaux *et al.* [27] used a spectral multidomain technique, whereas Sohankar *et al.* [30] used a finite volume method on a collocated grid to solve the incompressible Navier-Stokes equations for this test case. In order to deal with both challenges mentioned above, we use a nested grid approach, where the cylinder is embedded in a fine grid, which itself is embedded in a coarser grid (cf. Fig. 19). The grid refinement procedure of Lätt [14] and Dupuis and Chopard [31] was used for the grid refinement. The boundary condition used for the walls of the cylinder is the no-slip B boundary condition (cf. Sec. IV and the bounce back rule). At the artificial boundary, we used the FD boundary condition of Lätt *et al.* [4]. Details of the numerical setup of the present simulations and of the simulations of the groups we compare our results to are presented in Table V. Among the important parameters of the simulation are the total length L of the computational

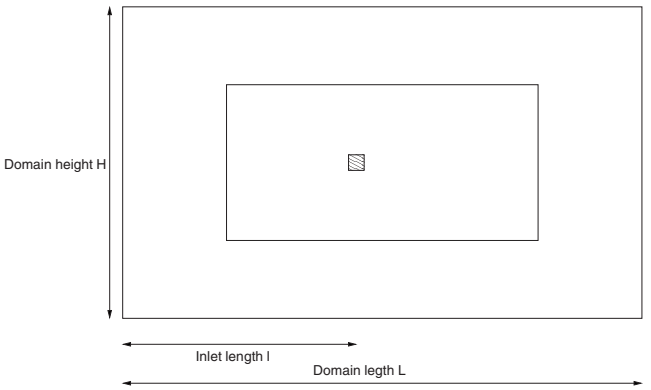

FIG. 19. Geometry of the numerical set up of the laminar unsteady flow around a square cylinder. The inner rectangle represents the finer grid with the cylinder inside whereas the outer rectangle is the computational domain wherein the finer grid is embedded.

TABLE V. Details of the setup of the flow past a square cylinder for the present simulation and reference simulations in the literature.

	$\delta x/D$	L/D	H/D	l/D
Ref. [28]	0.007	40	16	20.5
Ref. [29]		43	25	12.5
Ref. [27]		23	18	5.5
Ref. [30]	0.004	14–37	20 (40)	10.5
Present	0.025–0.1	84	40	33

domain, the distance from the inflow boundary condition to the cylinder l, the height of the computational domain H (cf. Fig. 19), and the grid spacing δx at the cylinder walls.

2. Numerical results

The numerical results for different resolutions are displayed in Table VI. Results for this case found in the literature are presented in Table VII. Sohankar *et al.* [30] emphasized that the root-mean-square value of the lift coefficient is a quantity highly sensitive to resolution and geometry. This can also be observed from the present results (cf. Table VI). The Strouhal number and the drag coefficient almost converged to the established values (cf. Table VII for a resolution of $N=40$), whereas the lift coefficient still exceeds the values in literature by approximately 20%. This holds true for both the present no-slip B boundary condition and the bounce back rule. When comparing the values of the Strouhal number, the mean drag coefficient, and the root-mean-square value of the lift coefficient for different resolutions (Table VI), we do not observe a quadratic convergence of the values to the established ones (Table VII). In the foregoing benchmark test (Sec. V E), we showed that the pressure field displays spurious oscillations around the step corner and that these oscillations have a negative effect on the order of convergence of our method. This might also be the cause for the present slow convergence.

For our simulation we used a relaxation frequency ω of 1.9417 which explains the very close agreement between the results by the no-slip B boundary condition and by the bounce back rule as mentioned above. However for a lower Reynolds number, i.e., a lower value of ω, the bounce back rule might not be as accurate anymore [8]. In general, other sources of errors might be dominating, such as the pressure oscillations around the corners, the errors introduced by the spatial discretization, or the artificial boundaries, which prevented us from reaching a grid independent solution. However, it is shown that the solution converges to the right values for the Strouhal number and the mean drag coefficient and that the root-mean-square value of the lift coefficient is converging into the right direction. Unfortunately additional simulations on finer grids exceeded our computational resources. Nevertheless, this benchmark test verifies the present boundary condition for a complex unsteady flow simulation.

TABLE VI. Strouhal number St, mean drag coefficient $\bar{C}_D$, and root-mean-square value of the lift coefficient $C_{L,\mathrm{rms}}$ for different resolutions N using the no-slip B boundary condition and the bounce back rule for the unsteady flow around a square cylinder at Re=100.

	N	St	$\bar{C}_D$	$C_{L,\mathrm{rms}}$
No-slip B	10	0.132	1.59	0.212
Bounce back	10	0.134	1.61	0.225
No-slip B	20	0.138	1.52	0.191
Bounce back	20	0.139	1.53	0.200
No-slip B	40	0.140	1.47	0.185
Bounce back	40	0.141	1.46	0.185

TABLE VII. Values of the Strouhal number St, the mean drag coefficient $\bar{C}_D$, and the root-mean-square value of the lift coefficient $C_{L,\mathrm{rms}}$ found in the literature.

	St	$\bar{C}_D$	$C_{L,\mathrm{rms}}$
Ref. [28]	0.143	1.47	0.157
Ref. [29]	0.144	1.44	0.152
Ref. [27]	0.154	1.53	
Ref. [30]	0.146	1.47	0.156

VI. ANALYSIS OF THE NO-SLIP BOUNDARY CONDITIONS

First we analyze the present no-slip boundary condition in Sec. VI A and consider then its relation to other boundary conditions (Sec. VI).

A. Multiscale analysis of the present no-slip condition

In this section, we perform a multiscale analysis, as explained in Sec. II for the present no-slip boundary condition, using formula (2.14) for the given populations. The computation of $\Pi^{(1)}=\Sigma_i \vec{c}_i\vec{c}_i f_i^{neq}$ for the present boundary conditions at the boundary node leads to

$$\Pi_{xx}^{(1)}=0, \tag{6.1}$$

$$\Pi_{yy}^{(1)}=0, \tag{6.2}$$

$$\Pi_{xy}^{(1)}=2(f_3^{neq}-f_5^{neq})+(f_2^{neq}-f_6^{neq}). \tag{6.3}$$

The two first equations follow directly from construction, corresponding to $\partial_x u$ and $\partial_y v$ identically zero. For small Mach and Knudson numbers, it follows from formula (2.14) that

$$\Pi_{xy}^{(1)}=-\frac{c_s^2}{\omega}\rho(\partial_y u+\partial_x v) \tag{6.4}$$

for both the no-slip C and the no-slip B boundary conditions. The reason why the no-slip B condition is less accurate is due to a loss of information by imposing

$$f_2^{neq} = f_6^{neq} = 0.$$

B. Relation to other boundary conditions

The boundary conditions of Inamuro *et al.* [8] and Zou and He [12] and the no-slip C boundary condition are very similar concerning their accuracy. This can be explained when examining these for the case of $\vec{u}=0$. Using Eq. (4.31), we can rewrite Eqs. (4.66) and (4.67),

$$f_1^{neq} = f_4^{neq} + f_5^{neq} + \tfrac{1}{2}(f_6^{neq} - f_2^{neq}), \tag{6.5}$$

$$f_7^{neq} = f_4^{neq} + f_3^{neq} - \tfrac{1}{2}(f_6^{neq} - f_2^{neq}). \tag{6.6}$$

1. Boundary condition of Zou and He

Zou and He [12] took $f_i^{in} = f_i^{ps}$ for $i=0,2,3,4,5,6$ and made use of Eqs. (2.10) and (2.11) in order to find the wall density,

$$\rho^{wall} = f_0^{in} + f_2^{in} + f_6^{in} + 2(f_3^{in} + f_4^{in} + f_5^{in}). \tag{6.7}$$

In order to close the system they assumed that the nonequilibrium part of the wall normal populations is bounced back $f_8^{neq} = f_4^{neq}$. This closes the system by help of Eq. (2.13) and we obtain

$$f_8^{neq} = f_4^{neq}, \tag{6.8}$$

$$f_1^{neq} = f_5^{neq} + \tfrac{1}{2}(f_6^{neq} - f_2^{neq}), \tag{6.9}$$

$$f_7^{neq} = f_3^{neq} - \tfrac{1}{2}(f_6^{neq} - f_2^{neq}). \tag{6.10}$$

Assuming that their estimate of ρ^{wall} produces a similar value as ours, we see that the asymmetric part of the diagonal populations, which is a measure for the nondiagonal element of the strain tensor, is equal to the asymmetric part of our diagonal populations [Eqs. (6.5) and (6.6)]. This is why the estimate for the bending of the velocity profile at the wall $\partial_y u$ of the boundary condition of Zou and He, which is crucial for the correct shape of the profile, is equal to the estimate of the no-slip C boundary condition. More explicitly if we compute $\Pi_{xy}^{(1)}$ for the boundary condition of Zou and He at the boundary node, we find

$$\Pi_{xy}^{(1)} = \sum_i \vec{c}_{i,x}\vec{c}_{i,y} f_i^{neq}$$

$$= f_7^{in} - f_1^{in} + f_3^{in} - f_5^{in} = 2(f_3^{in} - f_5^{in}) + (f_2^{in} - f_6^{in}).$$

This is the same expression as for the no-slip C boundary condition. The diagonal elements of $\Pi^{(1)}$ are

$$\Pi_{xx}^{(1)} = 2(f_3^{neq} + f_5^{neq}) + f_2^{neq} + f_6^{neq},$$

$$\Pi_{yy}^{(1)} = 2(f_3^{neq} + f_4^{neq} + f_5^{neq}),$$

which has been shown by Lätt *et al.* by inserting Eq. (2.14) and using Eq. (2.15) to yield in the limit of small Mach and Knudsen numbers,

$$\Pi_{xx}^{(1)} = -\frac{2c_s^2\rho}{\omega}\partial_x u,$$

$$\Pi_{yy}^{(1)} = -\frac{2c_s^2\rho}{\omega}\partial_y v,$$

which vanish up to second order at the boundaries. However, these boundary conditions do not conserve mass. The mass streamed out during one time step is equal to

$$\rho^{in} - \rho^{out} = \omega(f_3^{in} + f_4^{in} + f_5^{in}) - \omega\tfrac{1}{6}\rho^{wall},$$

where the density at the wall is estimated by Eq. (6.7). For small Mach and Knudsen numbers we obtain

$$\rho^{in} - \rho^{out} = -2c_s^2\rho\partial_y v.$$

This means also that the present estimate of the density at the wall node [formula (4.41)] and the density estimated by Eq. (6.7) differ by $\partial_y v$, which is zero up to second order at the boundary node. If ρ^{wall} had been estimated by Eq. (4.41), these boundary conditions would be mass conserving.

2. Boundary condition of Inamuro et al.

Approach of Inamuro *et al.* [8] is more sophisticated. Based on elements of kinetic theory they assumed that the outgoing populations, in our case f_1^{in}, f_7^{in}, and f_8^{in}, should be equilibrium distribution functions with a counterslip velocity u' and a counterslip density ρ', so that the fluid velocity at the wall is the same as the wall velocity and the fluid density is given by Eq. (6.7). For a southern wall at rest this leads to

$$f_8^{in} = \frac{1}{9}\rho' - 6\frac{(f_6^{in} - f_2^{in} + f_5^{in} - f_3^{in})^2}{\rho'}, \tag{6.11}$$

$$f_1^{in} = \frac{1}{36}\rho' + 3\frac{(f_6^{in} - f_2^{in} + f_5^{in} - f_3^{in})^2}{\rho'} + \frac{1}{2}(f_6^{in} - f_2^{in} + f_5^{in} - f_3^{in}), \tag{6.12}$$

$$f_7^{in} = \frac{1}{36}\rho' + 3\frac{(f_6^{in} - f_2^{in} + f_5^{in} - f_3^{in})^2}{\rho'} - \frac{1}{2}(f_6^{in} - f_2^{in} + f_5^{in} - f_3^{in}), \tag{6.13}$$

where $\rho' = 6(f_3^{in} + f_4^{in} + f_5^{in})$, which coincides with the estimate of the wall density by our boundary conditions. We see that the asymmetric parts of f_1^{in} and f_7^{in} are equal to the ones of the present no-slip C boundary condition. That is to say for $\Pi_{xy}^{(1)}$ we get

$$\Pi_{xy}^{(1)} = \sum_i \vec{c}_{i,x}\vec{c}_{i,y} f_i^{neq} = (f_6^{in} - f_2^{in} + f_5^{in} - f_3^{in}) + f_3^{in} - f_5^{in}$$

$$= 2(f_3^{in} - f_5^{in}) + (f_2^{in} - f_6^{in}),$$

which is exactly the same as for the Zou and He and the no-slip C boundary condition. This explains their similarity in accuracy and the similar susceptibility to instabilities when applied to a fixed wall. For the diagonal elements, neglecting the nonlinear terms, we find

$$\Pi_{xx}^{(1)} = f_2^{neq} + \tfrac{4}{3}f_3^{neq} + \tfrac{1}{3}f_4^{neq} + \tfrac{4}{3}f_5^{neq} + f_6^{neq},$$

TABLE VIII. Values of u, v, and p for the no-slip B boundary conditions and for the reference simulation of Erturk at $x/h=6$.

	u		$\times 10^{-1} v$		p
y/h	Present	Erturk	Present	Erturk	Present
0.00	0.0000	0.0000	0.0000	0.0000	0.1476
0.10	−0.0894	−0.0889	0.0072	0.0071	0.1476
0.20	−0.1467	−0.1459	0.0234	0.0231	0.1476
0.30	−0.1680	−0.1668	0.0397	0.0391	0.1476
0.40	−0.1513	−0.1501	0.0476	0.0468	0.1476
0.50	−0.0976	−0.0965	0.0407	0.0399	0.1475
0.60	−0.0088	−0.0079	0.0155	0.0151	0.1475
0.70	0.1150	0.1157	−0.0288	−0.0287	0.1475
0.80	0.2765	0.2770	−0.0911	−0.0902	0.1475
0.90	0.4784	0.4786	−0.1672	−0.1654	0.1477
1.00	0.7150	0.7148	−0.2483	−0.2455	0.1481
1.10	0.9620	0.9615	−0.3205	−0.3167	0.1489
1.20	1.1780	1.1773	−0.3698	−0.3651	0.1501
1.30	1.3215	1.3205	−0.3880	−0.3827	0.1518
1.40	1.3676	1.3663	−0.3738	−0.3684	0.1536
1.50	1.3085	1.3069	−0.3298	−0.3245	0.1554
1.60	1.1476	1.1459	−0.2609	−0.2565	0.1568
1.70	0.9001	0.8987	−0.1769	−0.1737	0.1577
1.80	0.5971	0.5963	−0.0927	−0.0909	0.1581
1.90	0.2825	0.2824	−0.0268	−0.0263	0.1581
2.00	0.0000	0.0000	0.0000	0.0000	0.1580
ϵ		0.0008		2.1×10^{-4}	

$$\Pi_{yy}^{(1)} = 2(f_3^{neq} + f_4^{neq} + f_5^{neq}).$$

The last equation shows that Π_{yy} is the same for boundary condition of Zou and He and Inamuro *et al.* In the limit of small Mach and Knudsen numbers, an expression for $\Pi_{xx}^{(1)}$ can be found by inserting Eq. (2.14) and using Eq. (2.15),

$$\Pi_{xx}^{(1)} = -\frac{5}{3}\frac{\rho c_s^2}{\omega}\partial_x u. \tag{6.14}$$

This is again zero at the boundary (up to second order). Equation (6.14) corresponds, apart from a typing error to what Lätt *et al.* found in their analysis [4].

The mass loss for boundary conditions of Inamuro *et al.* is given by

$$\rho^{in} - \rho^{out} = \omega\tfrac{1}{6}(\rho' - \rho),$$

where the density at the wall is estimated by Eq. (6.7). This is the same as for boundary condition of Zou and He.

3. Boundary condition of Halliday et al. and Hollis et al.

Halliday *et al.* and later on Hollis *et al.* presented a general way to close the unknown populations for boundary conditions [6,18]. Although their approach is very similar to ours for the case of the no-slip condition, differences exist. In their eyes, our choice of f_3^{neq}, f_4^{neq}, and f_5^{neq} as free parameters is a forbidden choice because the determinant of the system of equations for the remaining f_i^{neq}, $i=0,1,2,6,7,8$, composed by the condition of collision invariance of density [Eq. (2.12)], the collision invariance of momentum [Eq. (2.13)], and Eq. (2.17) is zero,

$$M \cdot \vec{a} = \vec{b},$$

where the 6×6 matrix M and the six-dimensional vectors $\vec{a}$ and $\vec{b}$ are given by

$$M = \begin{pmatrix} 1 & 1 & 1 & 1 & 1 & 1 \\ 0 & 1 & 0 & 0 & 1 & 1 \\ 0 & -1 & -1 & 1 & 1 & 0 \\ 0 & 1 & 1 & 1 & 1 & 0 \\ 0 & 1 & 0 & 0 & 1 & 1 \\ 0 & -1 & 0 & 0 & 1 & 0 \end{pmatrix},$$

$$\vec{a}^T = (f_0^{neq}, f_1^{neq}, f_2^{neq}, f_6^{neq}, f_7^{neq}, f_8^{neq}),$$

and

TABLE IX. Values of u, v, and p for the no-slip B boundary conditions and for the reference simulation of Erturk and Gartling at $x/h=14$.

	u			$\times 10^{-2} v$			p	
y/h	Present	Erturk	Gartling	Present	Erturk	Gartling	Present	Gartling
0.00	0.0000	0.0000	0.0000	0.0000	0.0000	0.0000	0.3010	0.1889
0.10	0.2425	0.2381	0.2320	0.0178	−0.0029	−0.1180	0.3009	0.1888
0.20	0.4484	0.4407	0.4280	−0.0759	−0.1429	−0.5040	0.3007	0.1885
0.30	0.6361	0.6272	0.6130	−0.2665	−0.3806	−1.0000	0.3000	0.1876
0.40	0.8121	0.8035	0.7920	−0.4226	−0.5784	−1.4230	0.2986	0.1859
0.50	0.9629	0.9554	0.9480	−0.4932	−0.6852	−1.7480	0.2964	0.1831
0.60	1.0698	1.0644	1.0620	−0.4761	−0.6954	−1.9170	0.2933	0.1792
0.70	1.1173	1.1147	1.1180	−0.3820	−0.6159	−1.9250	0.2897	0.1746
0.80	1.0970	1.0975	1.1050	−0.2331	−0.4663	−1.7780	0.2860	0.1697
0.90	1.0101	1.0136	1.0240	−0.0627	−0.2795	−1.5070	0.2825	0.1652
1.00	0.8684	0.8742	0.8850	0.0893	−0.0973	−1.1650	0.2798	0.1615
1.10	0.6931	0.7001	0.7090	0.1850	0.0377	−0.8230	0.2778	0.1590
1.20	0.5097	0.5166	0.5220	0.2024	0.0970	−0.5440	0.2766	0.1574
1.30	0.3405	0.3464	0.3490	0.1472	0.0794	−0.3620	0.2760	0.1567
1.40	0.1989	0.2035	0.2040	0.0512	0.0126	−0.2680	0.2758	0.1563
1.50	0.0897	0.0931	0.0920	−0.0433	−0.0621	−0.2250	0.2757	0.1562
1.60	0.0124	0.0149	0.0150	−0.1019	−0.1090	−0.1930	0.2757	0.1562
1.70	−0.0344	−0.0326	−0.0320	−0.1100	−0.1114	−0.1470	0.2757	0.1562
1.80	−0.0517	−0.0505	−0.0490	−0.0757	−0.0753	−0.0860	0.2757	0.1562
1.90	−0.0400	−0.0394	−0.0380	−0.0261	−0.0257	−0.0270	0.2757	0.1562
2.00	0.0000	0.0000	0.0000	0.0000	0.0000	0.0000	0.2757	0.1562
ϵ		0.0042	0.0090		9.65×10^{-4}	6.516×10^{-3}		0.1166

$$\vec{b} = \begin{pmatrix} -f_3^{neq} - f_4^{neq} - f_5^{neq} \\ f_3^{neq} - f_4^{neq} - f_5^{neq} \\ f_3^{neq} - f_5^{neq} \\ -f_3^{neq} - f_5^{neq} \\ -f_3^{neq} - f_4^{neq} - f_5^{neq} \\ k\mathbf{S}_{xy} + f_3^{neq} - f_5^{neq} \end{pmatrix},$$

where we introduced the analytic result for the diagonal elements of the rate of strain tensor into the second member. It is definitely correct that the determinant of M is zero, as can easily be verified, but this does not imply that one cannot choose f_3^{neq}, f_4^{neq}, and f_5^{neq} as initially given. It rather states that one has to look for more general conditions which imply the above ones, namely, Eqs. (4.28)–(4.34). Therefore it is advantageous to adopt the mass conservation formulation of Chopard and Dupuis since it is compatible to this system of equations. The present boundary conditions thus satisfy the constraints mentioned in [6,18]. In addition to local information, Halliday *et al.* and Hollis *et al.* used a finite difference stencil to evaluate the rate of strain tensor using neighboring nodes. The strength of the present method is that it uses the known elements of the rate of strain tensor, i.e., the diagonal elements, to compensate the lack of information due to the populations not streamed in $(i=1,7,8)$. It is therefore not needed to evaluate the off-diagonal element of the rate of strain tensor by a finite difference scheme and allows a purely local formulation.

VII. CONCLUSIONS

Our aim was to increase the physical content of the no-slip boundary condition at walls at rest for the lattice Boltzmann BGK method. Therefore we derived, starting from physical arguments, a formulation for the no-slip condition at walls at rest. Indeed the no-slip boundary condition at a wall at rest implies that the diagonal elements of the rate of strain tensor vanish for an incompressible flow (Sec. IV A). This has direct consequences for the leading order term of the nonequilibrium part in the multiscale expansion (Sec. IV B) and allowed us also to find a set of conditions [Eqs. (4.28)–(4.34)] similar to what [6,18] did. After having examined two different mass conservation formulations [18,19], the one of Chopard and Dupuis, which is compatible to the set of conditions, was chosen in order to obtain a definition of the density at the wall. We were now able to solve the set of equations for the missing populations which led to two formulations, one for low Reynolds number flows with high

TABLE X. Values of u, v, and p for the no-slip B boundary conditions and for the reference simulation of Erturk and Gartling at $x/h=30$.

	u			$\times 10^{-2} v$			p	
y/h	Present	Erturk	Gartling	Present	Erturk	Gartling	Present	Gartling
0.00	0.0000	0.0000	0.0000	0.0000	0.0000	0.0000	0.3635	0.2459
0.10	0.1103	0.1104	0.1090	−0.0181	−0.0181	−0.0190	0.3635	0.2459
0.20	0.2201	0.2202	0.2180	−0.0617	−0.0615	−0.0650	0.3635	0.2459
0.30	0.3303	0.3303	0.3280	−0.1137	−0.1134	−0.1190	0.3635	0.2459
0.40	0.4407	0.4407	0.4380	−0.1578	−0.1574	−0.1660	0.3635	0.2459
0.50	0.5489	0.5487	0.5470	−0.1803	−0.1800	−0.1910	0.3635	0.2459
0.60	0.6500	0.6496	0.6490	−0.1732	−0.1731	−0.1850	0.3635	0.2459
0.70	0.7372	0.7367	0.7370	−0.1346	−0.1348	−0.1470	0.3635	0.2459
0.80	0.8033	0.8028	0.8040	−0.0690	−0.0696	−0.0810	0.3635	0.2459
0.90	0.8424	0.8418	0.8440	0.0144	0.0134	0.0030	0.3635	0.2459
1.00	0.8508	0.8503	0.8530	0.1036	0.1022	0.0950	0.3635	0.2459
1.10	0.8280	0.8277	0.8310	0.1857	0.1842	0.1800	0.3635	0.2459
1.20	0.7768	0.7766	0.7790	0.2489	0.2473	0.2450	0.3635	0.2459
1.30	0.7023	0.7023	0.7040	0.2842	0.2827	0.2830	0.3635	0.2459
1.40	0.6115	0.6117	0.6130	0.2872	0.2858	0.2880	0.3635	0.2459
1.50	0.5115	0.5118	0.5120	0.2586	0.2574	0.2600	0.3635	0.2459
1.60	0.4081	0.4085	0.4080	0.2051	0.2042	0.2070	0.3635	0.2459
1.70	0.3049	0.3053	0.3040	0.1379	0.1374	0.1400	0.3635	0.2459
1.80	0.2030	0.2033	0.2020	0.0713	0.0710	0.0720	0.3635	0.2459
1.90	0.1017	0.1020	0.1010	0.0203	0.0202	0.0210	0.3635	0.2460
2.00	0.0000	0.0000	0.0000	0.0000	0.0000	0.0000	0.3635	0.2460
ϵ		0.0003	0.0013		6.0×10^{-6}	4.9×10^{-5}		0.1176

accuracy and another one for high Reynolds number flows, slightly less accurate. The stability and accuracy issue could thus be reduced to the formulation of the closure for one parameter, namely, the difference of the tangential populations. We treated only two formulations, one taking this difference as initially given (high accuracy) and one reducing it to zero (increased stability). Future research will point out whether there exists a formulation combining both aspects. Additionally, it has to be investigated how to apply the developed concepts to a three-dimensional wall, where not only the number of conditions increases, one for the mass conservation, three for the velocity, and six for the strain rate tensor, but also the number of populations, 15, 19, or 27.

Two preceding benchmark tests confirm the second-order accuracy of our no-slip boundary conditions as well as that they comply with transient flow simulations. The application to the backward facing step flow at Re=800 as our third benchmark test shows that the present no-slip boundary conditions work well at a relatively high value of the relaxation frequency ω and can handle important phenomena related to boundary conditions, such as separation and reattachment points. These phenomena have been correctly captured by the present boundary condition, as was shown for the upper eddy. We point also out that the lattice Boltzmann method is not free of difficulties encountered by other numerical methods, namely, the spurious oscillations of the pressure field at the step corner which decreased the order of convergence of the method. This might also be the reason for a slower convergence of integral quantities such as the drag and lift coefficient for our last benchmark test, the unsteady flow around a square cylinder at Re=100. Nevertheless we could show that the values of these quantities are converging toward the established ones.

Last but not least, we analyzed the present boundary conditions and the ones of Inamuro *et al.* and of Zou and He, well known for their accuracy, in the case of the no-slip condition at walls at rest, and we could show that they make use of the same formulation for the generation of the off-diagonal element of the rate of strain tensor which explains the similar behavior of these two boundary conditions also observed by Lätt *et al.* [4].

ACKNOWLEDGMENTS

The author would like to thank Bastien Chopard and Mustafa Barri for interesting discussions and also Orestis Malaspinas for helping with programming issues. Thanks go

to Maria Fernandino for critical reading of the paper. The author is especially grateful to Bernhard Müller for his gentle guidance and supervision. The coding has been done using the open source lattice Boltzmann library OPENLB [15].

APPENDIX: TABLES OF u, v, and p PROFILES FOR THE BACKWARD FACING STEP FLOW

For more information, see Tables VIII–X.

[1] D. Hänel, *Einführung in Die Kinetische Theorie der Gase und Lattice-Boltzmann-Methoden* (Springer-Verlag, Berlin, 2004).
[2] S. Succi, *The Lattice Boltzmann Equation for Fluid Dynamics and Beyond* (Oxford Science, Oxford, 2001).
[3] D. A. Wolf-Gladrow, *Lattice-Gas Cellular Automata and Lattice Boltzmann Models* (Springer, New York, 2000).
[4] J. Lätt, B. Chopard, O. Malaspinas, M. Deville, and A. Michler, Phys. Rev. E **77**, 056703 (2008).
[5] P. A. Skordos, Phys. Rev. E **48**, 4823 (1993).
[6] I. Halliday, L. A. Hammond, and C. M. Care, J. Phys. A **35**, L157 (2002).
[7] X. He, Q. Zou, L.-S. Luo, and M. Dembo, J. Stat. Phys. **87**, 115 (1997).
[8] T. Inamuro, M. Yoshino, and F. Ogino, Phys. Fluids **7**, 2928 (1995).
[9] O. Filippova and D. Hänel, Int. J. Mod. Phys. C **9**, 1271 (1998).
[10] P. Lallemand and L.-S. Luo, J. Comput. Phys. **184**, 406 (2003).
[11] M. Junk and Z. Yang, Phys. Rev. E **72**, 066701 (2005).
[12] Q. Zou and X. He, Phys. Fluids **9**, 1591 (1997).
[13] S. Chen and G. D. Doolen, Annu. Rev. Fluid Mech. **30**, 329 (1998).
[14] J. Lätt, Ph.D. thesis, Université de Genève, 2007.
[15] The OPENLB project, http://www.lbmethod.org/openlb/, 2006.
[16] S. A. Orszag, M. Israeli, and M. O. Deville, J. Sci. Comput. **1**, 75 (1986).
[17] Paul A. Durbin and Björn A. Pettersson Reif, *Statistical Theory and Modeling for Turbulent Flows* (Wiley, Chichester, 2001).
[18] A. P. Hollis, I. Halliday, and C. M. Care, J. Phys. A **39**, 10589 (2006).
[19] B. Chopard and A. Dupuis, Int. J. Mod. Phys. B **17**, 103 (2003).
[20] Z. Guo, B. Shi, and C. Zheng, Int. J. Numer. Methods Fluids **39**, 325 (2002).
[21] Z. Guo, C. Zheng, and B. Shi, Phys. Rev. E **65**, 046308 (2002).
[22] I. G. Currie, *Fundamental Mechanics of Fluids* (McGraw-Hill, New York, 1974).
[23] K. Morgan, J. Periaux, and F. Thomasset, *Analysis of Laminar Flow Over a Backward Facing Step* (Vieweg, Braunschweig, 1984).
[24] D. K. Gartling, Int. J. Numer. Methods Fluids **11**, 953 (1990).
[25] E. Erturk, Comput. Fluids **37**, 633 (2008).
[26] J. Keskar and D. A. Lyn, Int. J. Numer. Methods Fluids **29**, 411 (1999).
[27] J. Robichaux, S. Balachandar, and S. P. Vanka, Phys. Fluids **11**, 560 (1999).
[28] A. Lankadasu and S. Vengadesan, Int. J. Heat Fluid Flow **29**, 1054 (2008).
[29] M. Cheng, D. S. Whyte, and J. Lou, J. Fluids Struct. **23**, 207 (2007).
[30] A. Sohankar, C. Norberg, and L. Davidson, Int. J. Numer. Methods Fluids **26**, 39 (1998).
[31] A. Dupuis and B. Chopard, Phys. Rev. E **67**, 066707 (2003).